Monthly Notices of the ROYAL ASTRONOMICAL SOCIETY

MNRAS **485,** 3334–3351 (2019) doi:10.1093/mnras/stz603
Advance Access publication 2019 March 14

Star formation in IRDC G31.97+0.07

Chenlin Zhou [1,2,3]★ Ming Zhu,[1,3]★ Jinghua Yuan,[1] Yuefang Wu,[4] Lixia Yuan,[1,2,3] T. J. T. Moore[5] and D. J. Eden [5]

[1]*National Astronomical Observatories, Chinese Academy of Sciences, 20A Datun Road, Chaoyang District, Beijing 100012, China*
[2]*University of Chinese Academy of Sciences, Beijing 100049, China*
[3]*Key Laboratory of FAST, NAOC, Chinese Academy of Science, Beijing 100012, China*
[4]*Department of Astronomy, Peking University, 100871 Beijing, China*
[5]*Astrophysics Research Institute, Liverpool John Moores University, IC2, Liverpool Science Park, 146 Brownlow Hill, Liverpool L3 5RF, UK*

Accepted 2019 February 22. Received 2019 February 22; in original form 2018 May 23

ABSTRACT

We utilize multiple-waveband continuum and molecular-line data of CO isotopes to study the dynamical structure and physical properties of the IRDC G31.97+0.07. We derive the dust temperature and H_2 column density maps of the whole structure by spectral energy distribution fitting. The total mass is about $2.5 \times 10^5\,M_\odot$ for the whole filamentary structure and about $7.8 \times 10^4\,M_\odot$ for the infrared dark cloud (IRDC). Column density probability distribution functions (PDFs) produced from the column density map are generally in the power-law form, suggesting that this part is mainly gravity dominant. The flatter slope of the PDF of the IRDC implies that it might be compressed by an adjacent, larger H II region. There are 27 clumps identified from the 850 μm continuum located in this filamentary structure. Based on the average spacing of the fragments in the IRDC, we estimate the age of the IRDC. The age is about 6.4 Myr, assuming inclination angle $i = 30°$. For 18 clumps with relatively strong CO and ^{13}CO (3–2) emission, we study their line profiles and stabilities. We find five clumps with blue profiles that indicate gas infall motion and two clumps with red profiles that indicate outflows or expansion. Only one clump has $\alpha_{\rm vir} > 2$, suggesting that most clumps are gravitationally bound and tend to collapse. In the mass–$R_{\rm eq}$ diagram, 23 of 27 clumps are above the threshold for high-mass star formation, suggesting that this region can be a good place for studying high-mass star forming.

Key words: stars: formation – ISM: clouds – ISM: kinematics and dynamics – ISM: structure.

1 INTRODUCTION

Massive stars ($M \geq 8M_\odot$) and massive stellar clusters play an important role in moulding the galactic environment and determining the metal enrichment through their ionizing radiation, stellar winds, outflows, and explosive deaths. However, much remains to be understood about the formation and protostellar evolution of high-mass stars. The initial conditions and the earliest evolutionary stages of massive star formation are still unclear.

Infrared dark clouds (IRDCs) have been proposed to be good candidates for the birthplaces of massive stars and clusters. IRDCs were first observed as dark silhouettes against the bright Galactic background infrared (IR) emission by the *Midcourse Space Experiment* (MSX; Carey et al. 1998; Egan et al. 1998; Simon et al. 2006), and the *Infrared Space Observatory* (Hennebelle et al. 2001). Previous molecular lines and continuum studies suggested that IRDCs were cold (< 20 K) and dense (> 10^5 cm^{-3}) gas collections, typically arranged in filamentary and/or globular structures with compact cores. Their masses range from 10^2 to $10^5\,M_\odot$ with a scale of several to tens of pc (Carey et al. 1998; Egan et al. 1998; Rathborne, Jackson & Simon 2006). All of these properties imply that IRDCs are an excellent mass reservoir for massive star formation.

The filamentary IRDC can be seen as a self-gravitating gas cylinder. Theoretical work predicted that the filament should fragment into multiple cores with quasi-regular spacing due to the 'sausage' instability (Chandrasekhar & Fermi 1953; Nagasawa 1987; Inutsuka & Miyama 1992; Tomisaka 1995). That was approved by observational studies showing that many cores/clumps were embedded in filamentary IRDCs (Rathborne et al. 2006; Wang et al. 2008; Henning et al. 2010; Jackson et al. 2010; Wang et al. 2014). In addition, recent studies have revealed massive young stellar objects (YSOs) and cores in IRDCs (Rathborne et al. 2006; Beuther &

★ E-mail: zhouchenlin@nao.cas.cn (CZ); mz@nao.cas.cn (MZ)

Steinacker 2007; Rathborne, Simon & Jackson 2007; Wang et al. 2008;; Henning et al. 2010; Rathborne et al. 2011), indicating that IRDCs are active subjects with undergoing massive star formation.

G31.97+0.07 was first identified by *MSX* (Simon et al. 2006). The IR morphology has a long, thin filamentary structure, and it is located in the west side of an active star-forming complex containing several (UC)H II regions (see Fig. 1 in Section 2.1). The central velocity of the IRDC is 96.7 km s^{-1} given by Simon et al. (2006). The central velocity and position are well consistent with the molecular cloud GRSMC G032.09+00.09 (Roman-Duval et al. 2009). So in this work, we use the distance of GRSMC G032.09+00.09 for our object. The distance is 7.07 kpc, using the Clemens rotation curve of the Milky Way (Clemens 1985) and solving the kinematic distance ambiguity by H I self-absorption analysis.

Rathborne et al. (2006) observed nine dense clumps with masses ranging from 151 to 1890 $M_\odot$ using the IRAM 30 m single-dish telescope. Wang et al. (2006) reported water masers in G31.97+0.07, and Urquhart et al. (2009) identified an H II region in G31.97+0.07. Battersby et al. (2014) studied G31.97+0.07 in the NH_3 (1,1), (2, 2), and (4,4) transitions with the Very Large Array (VLA). They identified 11 dense cores less 0.1 pc in size, and found that those cores were virially unstable to gravitational collapse. They also reported that turbulence likely set the fragmentation length scale in the filament. Moreover, they note the existence of at least three large bubbles around the filament, which are likely older H II regions. They suggested that those large H II regions may have compressed the molecular gas to form and/or shape the IRDC and trigger more recent massive star formation. Using the IRAM 30 m and CSO 10.4 m telescopes, Zhang et al. (2017) performed observations with HCO^+, HCN, N_2H^+, $C^{18}O$, DCO^+, SiO, and DCN towards G31.97+0.07. They reported that $C^{18}O$ emission may be heavily depleted at the peak positions of some cold cores. And they suggest that some active cores are collapsing while their envelopes are expanding.

In this work, we utilize multiple wavebands of continuum data (from Mid-IR to 850 μm), and molecular line data of three CO isotopes at $J = 1 \rightarrow 0$ and $J = 3 \rightarrow 2$ transition, to study the dynamical structure of IRDC G31.97+0.07 and star formation processes in dense clumps embedded in the structure. The data used in this work are described in Section 2. We present results of large-scale cloud and the dust and gas properties derived from continuum and molecular lines data in Section 3. Further discussion about gas dynamics and dense clumps properties is given in Section 4. We summarize our work in Section 5.

2 OBSERVATIONS AND DATA REDUCTION

2.1 IR to sub-millimetre continuum data

We utilized near-IR and mid-IR data from the GLIMPSE and MIPSGAL survey. The GLIMPSE survey observed the Galactic plane with four IR bands (3.6, 4.5, 5.8, 8.0 μm) of the IRAC instrument on the *Spitzer Space Telescope*, and the sky coverage is $|b| < 1^\circ$ for $10^\circ < \ell < 65^\circ$ (Benjamin et al. 2003; Churchwell et al. 2009). MIPSGAL is a survey of the same area as GLIMPSE, using MIPS instrument at 24 and 70 μm on *Spitzer* (Carey et al. 2009). The point-source catalogue from GLIMPSE (Spitzer Science 2009) and 24 μm point-source catalogue from MIPSGAL (Gutermuth & Heyer 2015) have been used to identify YSO candidates.

Far-IR data were obtained from the Hi-GAL survey to investigate dust properties of our object. Hi-GAL (*Herschel* Infrared Galactic Plane Survey; Molinari et al. 2010) is a key project of *Herschel* Space Observatory that mapped the entire Galactic plane with $|b| \leq 1^\circ$. The Hi-GAL data were observed in the fast mode using the PACS (70 and 160 μm) and SPIRE (250, 350, 500 μm) instruments in the parallel mode. We used the *Herschel* Interactive Processing Environment (HIPE) to download the continuum maps from the *Herschel* Science Archive and to reduce the data using standard pipelines. The effective angular resolution is 10.2, 13.5, 18.1, 24.9, and 36.4 arcsec at 70, 160, 250, 350, and 500 μm, respectively. In addition, the 70 μm point-source catalogues from Hi-GAL (Molinari et al. 2016a) were used to investigate evolutionary stages of the clumps in our object.

We extracted 850 μm continuum data from the James Clerk Maxwell Telescope (JCMT) Plane Survey (JPS; Moore et al. 2015; Eden et al. 2017). JPS is a targeted, yet unbiased, survey of the inner Galactic plane in the longitude range $7^\circ < \ell < 63^\circ$ and latitude range $|b| < 0.8^\circ$ using Sub-millimetre Common-User Bolometer Array 2 (SCUBA-2; Holland et al. 2013) at 850 μm with an angular resolution of 14.5 arcsec. The survey observing strategy is to map six large, regularly spaced fields within the area. Each individual survey field is sampled using a regular grid of eleven circular tiles with a uniform diameter of one degree, observed using the *pong*3600 mode (Bintley et al. 2014). The data reduction process removes structures larger than 480 arcsec from the final maps, which are gridded to 3 arcsec per pixel. The average smoothed pixel-to-pixel noise is 7.19 mJy beam^{-1}. The JPS 850 μm compact-source catalogue identified by Eden et al. (2017) using the FELLWALKER algorithm (Berry 2015) is also adopted in this study.

2.2 Molecular line data

^{13}CO (1–0) emission data from the Boston University-Five College Radio Astronomy Observatory Galactic Ring Survey (BU-FCRAO GRS; Jackson et al. 2006) were used to identify large-scale structures. The survey covered a longitude range of $18^\circ < \ell < 55.7^\circ$ and a latitude range of $|b| < 1^\circ$, using the SEQUOIA multipixel array on the Five College Radio Astronomy Observatory 14 m telescope. The velocity resolution of the survey is 0.21 km s^{-1}, and angular resolution is 46 arcsec. The typical rms sensitivity is $\sigma(T_A^*) \sim 0.13$K.

We used CO (3–2) data from the CO High Resolution Survey (COHRS; Dempsey, Thomas & Currie 2013) to study warm and high-velocity gas that may be excited by shocks and outflows from active star-forming regions. This survey covers $|b| < 0.5^\circ$ between $10^\circ < \ell < 65^\circ$ using the HARP instrument on the JCMT. The final data cube were smoothed to the angular resolution of 16.6 arcsec and rebinned to 1 km s^{-1}. The mean rms is about 1 K and a main-beam efficiency of $\eta_{\rm mb} = 0.61$.

Data from the $^{13}CO/C^{18}O$ (3–2) Heterodyne Inner Milky-Way Plane Survey (CHIMPS: Rigby et al. 2016) were used to investigate the denser part (e.g. clumps embedded in the structure). CHIMPS was carried out using the HARP on the JCMT, observing ^{13}CO and $C^{18}O$ (3–2) simultaneously. The survey covers $|b| \leq 0.5^\circ$ and $28^\circ \lesssim \ell \lesssim 46^\circ$, with an angular resolution of 15 arcsec in 0.5 km s^{-1}. The mean rms of the data is about 0.6 K and a main-beam efficiency of $\eta_{\rm mb} = 0.72$.

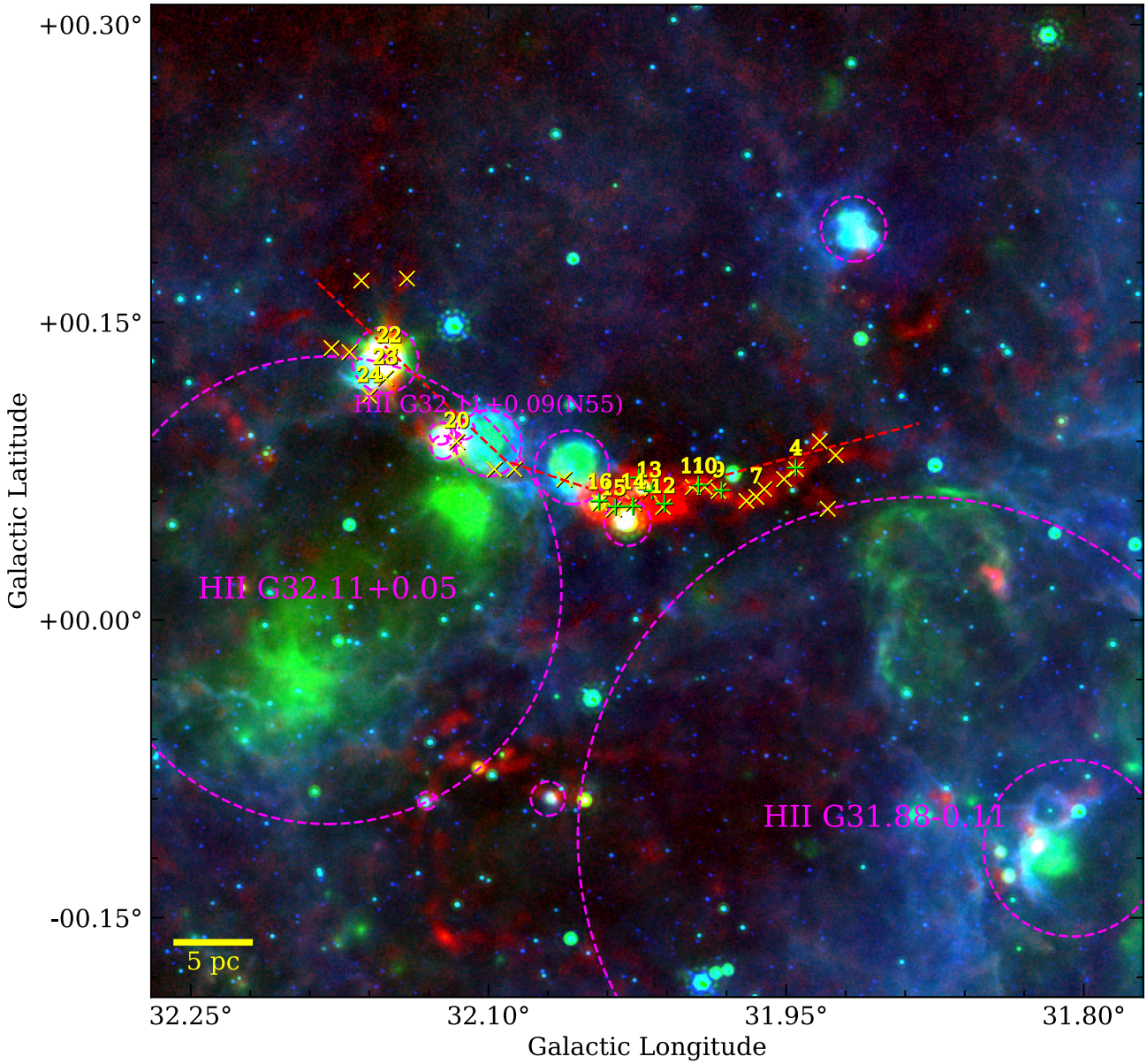

Figure 1. The three-colour image for IRDC G31.97+0.07 at large scale, red: JPS 850 μm, green: MIPSGAL 24 μm, blue: GLIMPSE 8 μm. Red dashed lines mark the filamentary structure. The IRDC displays the extinction feature at near/mid-IR wavebands but emits at sub-millimetre wavelengths. The magenta dashed circles represent the positions of H II regions identified by Anderson et al. (2014). Green crosses show the positions of the millimetre cores MM1–MM9 identified by Rathborne et al. (2006) and yellow crosses show the positions of 27 JPS compact sources identified by Eden et al. (2017). The IDs of JPS clumps with signal-noise ratio at 850 μm larger than 10 are labelled.

3 RESULTS

3.1 IR and sub-millimetre continuum emission

Fig. 1 displays the three-colour image (red: JPS 850 μm, green: MIPSGAL 24 μm, blue: GLIMPSE 8 μm) of the filamentary IRDC G31.97+0.07 and its adjacent context. The filamentary structure is marked by the red-dashed line, and H II regions identified by Anderson et al. (2014) from Wide-field Infrared Survey Explorer (*WISE*) data are shown in magenta dashed circles. In Fig. 1, the filamentary structure is divided into two parts: the eastern near/mid-IR dominant part and western sub-millimetre dominant part. The bright 8 μm emission is mainly attributed to polycyclic aromatic hydrocarbons excited by the UV radiation in the adjacent H II region (Pomarès et al. 2009). Thus, 8 μm emission can be utilized to delineate infrared bubbles. The eastern part, located on the rim of the large H II region G32.11+0.05, contains several 8 μm-bright H II regions: H II G32.16+0.13, H II G32.11+0.09 (or bubble N55 in Churchwell et al. 2006), and H II G32.06+0.08. This indicates that the eastern part hosts some young O or B type stars with strong stellar winds. Two UC H II regions located on the rim of N55 may suggest efficient star-forming in this region. The western part, mainly consisting of IRDC G31.97+0.07 and some other small filaments, displays a dark extinction feature. The green crosses show the positions of 9 cores, MM1–MM9, identified in 1.2 mm continuum data by Rathborne et al. (2006) using the IRAM 30 m telescope. The yellow crosses show the positions of 27 JCMT

compact sources identified by Eden et al. (2017) from JPS 850 μm data.

The 24 μm continuum emission is mainly contributed by the thermal radiation of warm dust heated by protostars (Battersby et al. 2011; Guzmán et al. 2015). H II regions and infrared bubbles, distributed in the filamentary structure, exhibit strong emission in their inner regions in the 24 μm waveband. IRDC 31.97+0.07 mostly appears as dark extinction at 24 and 70 μm. Some of the mm continuum cores identified by Rathborne et al. (2006) and sub-millimetre compact sources identified by Eden et al. (2017) do not show 24 μm emission, indicating that they are cold and dense. Battersby et al. (2014) divided the IRDC into two parts, the 'active part' and the 'quiescent part'. MM1, MM2, MM3, MM6, and MM9, belonging to the 'active part', are associated with mid-IR bright point sources. This suggests that these cores are undergoing star formation and heating the nearby dust.

Sub-millimetre continuum emission can be a good tracer of the cold and dense dust. It also can be an effective tool to search for clumps lacking signs of the star-forming process, or in early evolutionary stage. The long filament of IRDC G31.97+0.07 can be easily distinguished in the 850 μm image. The Bubble N55 and H II G32.06+0.08 are devoid of 850 μm emission, while other H II regions in the IRDC are associated with bright 850 μm clumps. This indicates that bubble N55 and H II G32.06+0.08 are more evolved than other H II regions in the filament. Considering the morphology in the continuum emission, we suggest that IRDC 31.97+0.07 and the H II regions on its east side may be one continuous structure, which is further confirmed by the continuity of velocity (see in Section 3.2).

3.2 CO molecular line emission

We use GRS ^{13}CO (1–0) molecular line emission to show the gas distribution of IRDC G31.97+0.07. Fig. 2 shows the ^{13}CO channel maps overlaid on 8 μm emission in steps of 1 km s^{-1}, between 90 and 101 km s^{-1}. Most ^{13}CO emission is detected in the velocity interval of 93–99 km s^{-1}, while UC H II regions and the 'active' clumps in the IRDC contain high-velocity components that may be driven by outflows from YSOs. The channel maps also show that IRDC G31.97+0.07 and the H II regions on its east side belong to the continuous filamentary structure also implied by continuum emission data, with a systemic velocity at 96.5 km s^{-1}.

Fig. 3 shows contours of GRS ^{13}CO (1–0) integrated intensity overlaid on 8 and 850 μm continuum emission. The velocity interval is between 90 and 101 km s^{-1}, with central velocity 96.5 km s^{-1}. The red dashed line marks the filamentary structure. The ^{13}CO (1–0) integrated map shows the molecular cloud GRSMC G032.09+00.09 identified by Rathborne et al. (2009) with central velocity 96.85 km s^{-1} (Roman-Duval et al. 2009). The shape of the dense and gas-rich part of GRSMC G032.09+00.09 is consistent with the filamentary structure of the continuum. That suggests that IRDC 31.97+0.07 and the H II regions on its east side are one continuous structure embedded in the molecular cloud GRSMC G032.09+00.09, and the distance of the cloud is 7.07 kpc (Roman-Duval et al. 2009). The length of the whole filamentary structure is about 20 arcmin and ∼41 pc at this distance. The radii of the JPS compact sources located in the structure range from 0.2 to 0.8 pc; hence, they are molecular clumps.

3.3 Spectral energy distribution fitting

To determine the properties of the dust, we fit the spectral energy distribution (SED) of our object pixel by pixel based on *Herschel* data. As the most part of the IRDC is 70 μm dark, we just take emission at 160, 250, 350, 500 μm into account in our SED fitting.

In order to measure the flux of multiwaveband observations in different angular resolutions, we convolved our image to a common angular resolution by a Gaussian kernel with full width at half-maximum (FWHM) equal to $\sqrt{\theta_{500}^2 - \theta_\lambda^2}$, where θ_{500} is FWHM beam size of Hi-GAL 500 μm band and θ_λ is the FWHM beam size of each Hi-GAL band. Then we re-gridded our data to be aligned pixel by pixel with the same pixel size of 14 arcsec.

We used the smoothed data to fit the SED for each pixel by using a grey-body model:

$$I_\nu = B_\nu(T_d)(1 - \mathrm{e}^{-\tau_\nu}), \tag{1}$$

where I_ν is the monochromatic intensity, $B_\nu(T_d)$ is the Planck function, and τ_ν, the optical depth at frequency ν, is given by

$$\tau_\nu = \mu_{\mathrm{H_2}} m_\mathrm{H} \kappa_\nu N_{\mathrm{H_2}}/\mathrm{GDR}. \tag{2}$$

Here, $\mu_{\mathrm{H_2}} = 2.8$ is the mean molecular weight of molecular hydrogen (Kauffmann et al. 2008), m_H is the mass of a hydrogen atom, $N_{\mathrm{H_2}}$ is the column density of H_2, GDR is the gas-to-dust ratio by mass and is assumed to be 100. The dust opacity κ_ν can be approximated by a power law,

$$\kappa_\nu = \kappa_{\nu_0} \left(\frac{\nu}{\nu_0}\right)^\beta, \tag{3}$$

where $\nu_0 = 600$ GHz, β fixed to be 2.0 is the dust emissivity index, and $\kappa_{\nu_0} = 3.33$ cm^2 g^{-1} (from column 5 of table 1 in Ossenkopf & Henning 1994), but scaled down by a factor of 1.5 as suggested in Kauffmann et al. (2010).

The fitting is performed by using CURVE_FIT in the PYTHON package SCIPY.OPTIMIZATION.[1] For pixels with intensity in 160 μm lower than 60 MJy sr^{-1} (about 3σ), we found that the fitting result was not so reliable. So, for those pixels, only 250, 350, 500 μm data were used in fitting.

The dust temperature and column density maps produced by SED fitting are presented in Fig. 4. The dust temperature of the whole filamentary structure ranges from 10 to 30 K, and the column density ranges from 0.5 × 10^{22} to 10^{23} cm^{-2}. Most of the IRDC is cold (lower than 18 K) with relatively high column density (above 2 × 10^{22} cm^{-2}), while the H II and UC H II regions have higher dust temperature and lower column density.

We find that the contour of 1.1 × 10^{22} cm^{-2} is similar to the CO integrated map of the cloud, and the contour of 1.8 × 10^{22} cm^{-2} is consistent with the morphology of the IRDC G31.97+0.07 in IR maps. So, choosing those values as thresholds, we derive that the mass of the whole structure is ∼2.5 × 10^5 M$_\odot$ and the mass of the IRDC is ∼7.8 × 10^4 M$_\odot$.

The clump mass and dust temperature can be directly derived from the SED fitting result:

$$M_\mathrm{clump} = \mu_{\mathrm{H_2}} m_\mathrm{H} d^2 \Omega_\mathrm{pix} \sum N_{\mathrm{H_2}}, \tag{4}$$

here, $d = 7.07$ kpc is the distance of the filament structure, Ω_pix is solid angular size of one pixel and $\sum N_{\mathrm{H_2}}$ is the sum of the column density value for all the pixels in the clump.

[1] https://docs.scipy.org/doc/scipy/reference/tutorial/optimize.html

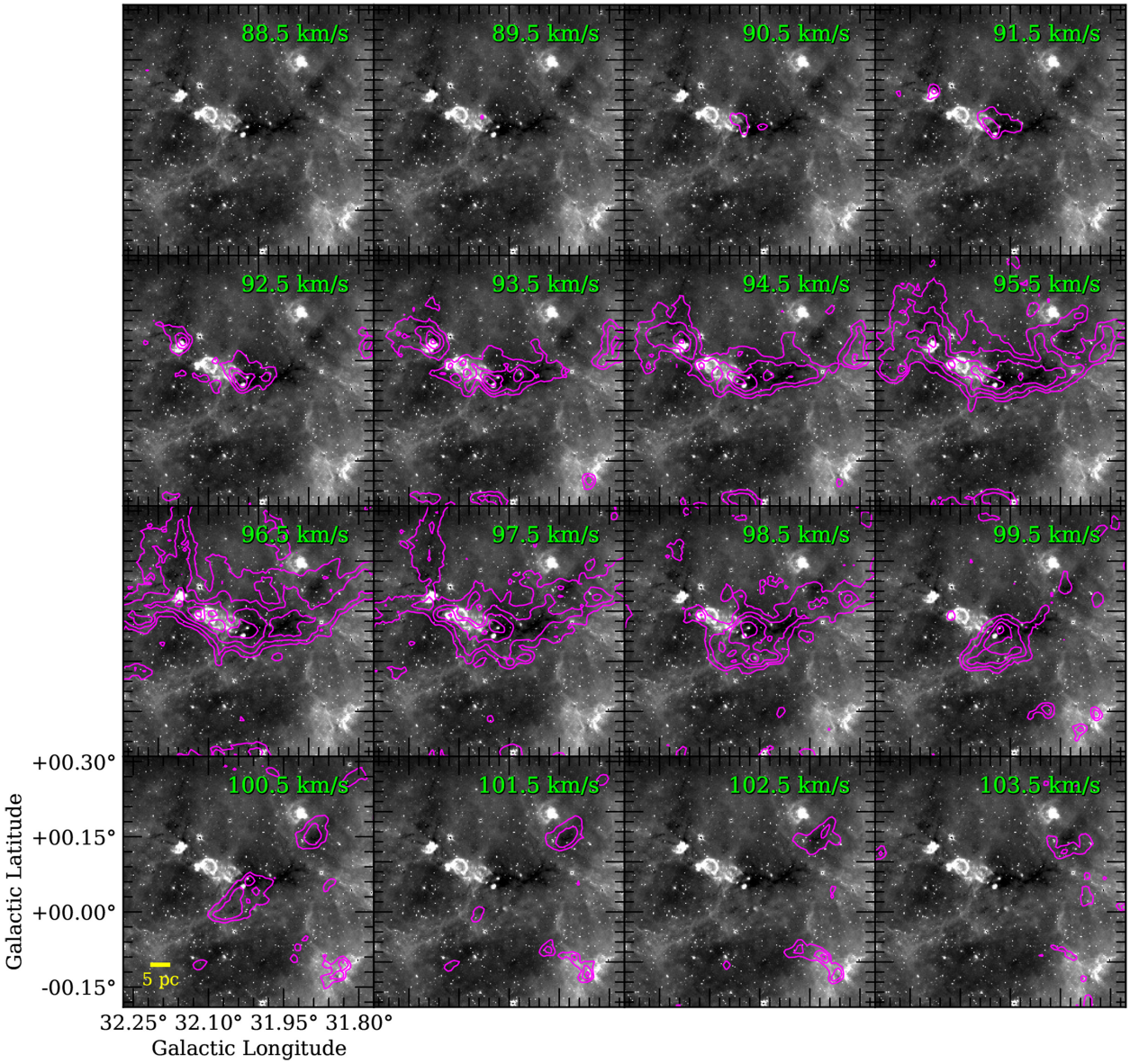

Figure 2. GRS ^{13}CO (1–0) channel maps in steps of 1 km s^{-1}. The background is *Spitzer*-IRAC 8 μm continuum emission. Central velocities are shown in each map.

The source average H_2 column densities are calculated as

$$N_{H_2} = \sum N_{H_2}/N_{sour}, \quad (5)$$

where N_{sour} is the number of pixels located in the clump. The average H_2 volume densities are derived via

$$n_{H_2} = \frac{M_{clump}}{(4/3)\pi r_{eq}^3 \mu_{H_2} m_H}, \quad (6)$$

and the mass surface densities are given by

$$\Sigma_{mass} = \frac{M_{clump}}{\pi r_{eq}^2}, \quad (7)$$

where r_{eq} is the equivalent radius.

We also determined the integrated intensity in the SED fitting process, so luminosities of sources are derived from

$$L_{clump} = 4\pi d^2 \Omega_{pix} \sum I_{int}, \quad (8)$$

where $\sum I_{int}$ is the sum of the frequency-integrated intensity($I_{int} = \int I_\nu \, d\nu$) for each pixel in the clump. And the luminosity–mass ratio is given by

$$L/M \text{ ratio} = L_{clump}/M_{clump}. \quad (9)$$

Table 1 lists the resulting dust temperature, column density, volume density, mass surface density, mass, luminosity, and luminosity–mass ratio of each source.

3.4 Distribution of YSOs

We selected sources with 3.6, 4.5, 5.8, 8.0 μm emission from the GLIMPSE I point-source catalogue (Spitzer Science 2009) to identify YSOs. Classification was performed using the method given in appendix A of Gutermuth et al. (2009). In brief, the method uses flux ratios or colours to classify YSO candidates into Classes

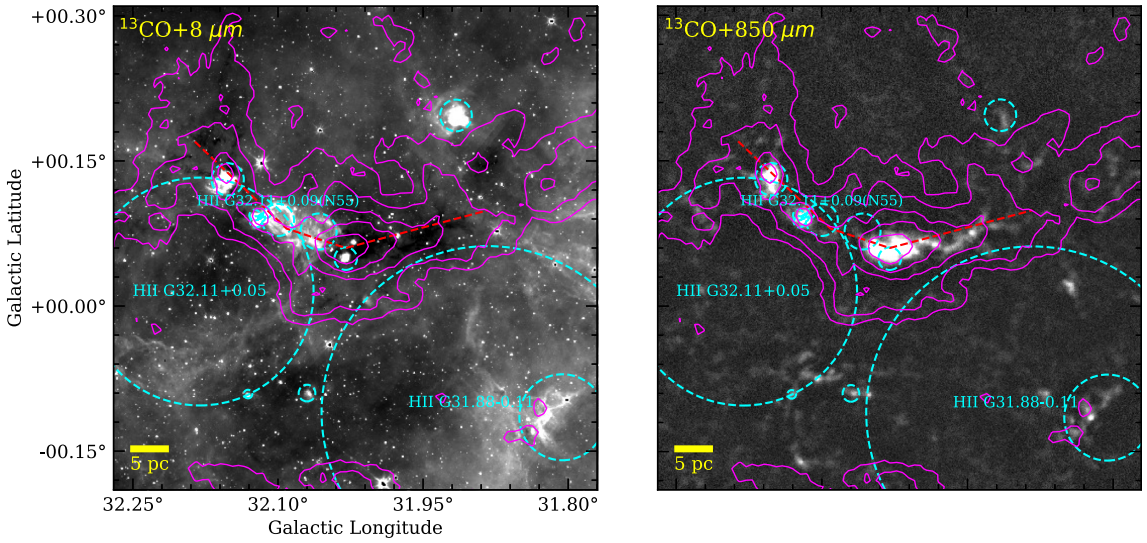

Figure 3. Contours of the GRS ^{13}CO (1–0) integrated map overlaid on *Spitzer* 8 μm emission map(left) and JCMT 850 μm emission map (right). The integrated velocity is from 90 to 101 km s^{-1}. The contour levels are [0.1, 0.2, 0.35, 0.5, 0.75] × 31.9 K km s^{-1}. The red dashed line marks the filamentary structure. Cyan dashed circles represent the positions of H II regions identified by Anderson et al. (2014).

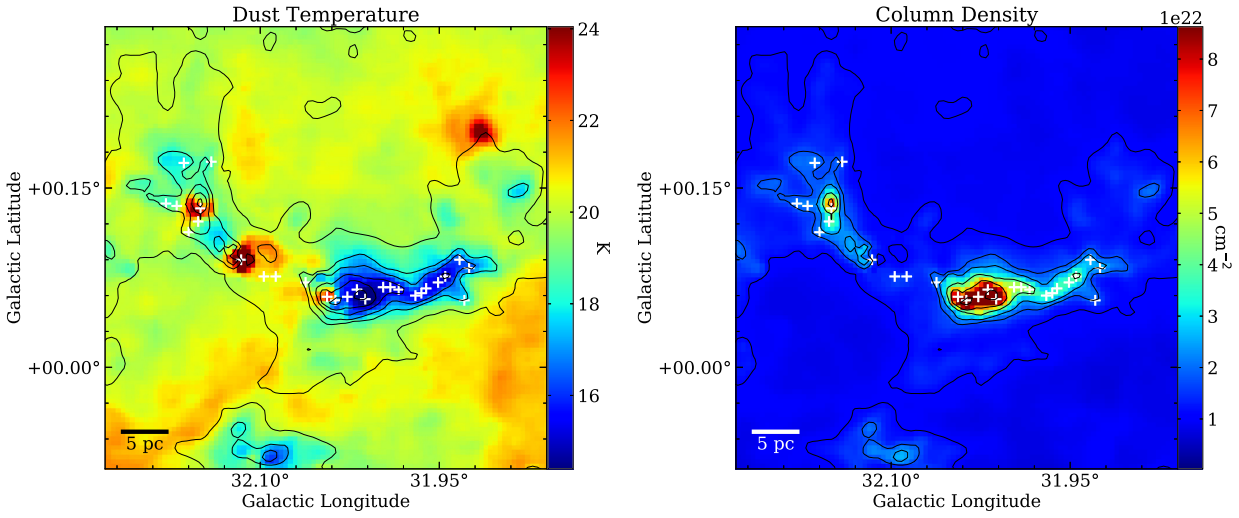

Figure 4. The dust temperature (left) and the H_2 column density (right) maps produced by SED fitting. White crosses show the JPS compact continuum sources. The contour levels are [1.1, 1.8, 2.4, 4.0, 6.5, 11.5] × 10^{22} cm^{-2}.

I and II, after excluding contamination like star-forming galaxies, broad-line active galactic nuclei (AGNs), and unresolved knots of shock emission. The result of the YSO identification is shown in Fig. 5. Also, 24 and 70 μm point sources can be considered as the signature of early-stage star formation; hence, we plot them in Fig. 5 to show the star-formation process in the area more completely. 24 μm point sources come from Gutermuth & Heyer (2015) and 70 μm point sources come from Molinari et al. (2016a).

We classify JPS clumps in the filament into two groups: protostellar clumps, which are associated with any YSOs, 24 or 70 μm point sources, and starless clumps, which are not. These two groups of clumps are shown in Fig. 5, with protostellar clumps as green ellipses and starless clumps as yellow ellipses. We identify 9 starless clumps and 18 protostellar clumps. Most of starless clumps are located along the IRDC, while most of protostellar clumps are distributed in the active star-forming area. The distribution of JPS clumps indicates that, along the filament, the evolutionary stages of star formation vary from the east to the west. The H II regions and IR bubbles that are more highly evolved are located in the east of the filament, while the west of the filament is quiescent. The IRDC can be divided into two parts, the *active part* and the *quiescent part* as mentioned in Battersby et al. (2014). The active part, containing plenty of YSOs and mid-IR point sources, displays signs of active star formation. While the quiescent part, in which most of clumps are starless, shows weak star-forming activity at present. Most of the protostellar clumps are distributed in the highly evolved part (around H II regions or in active part of the IRDC). But, in our work, it is hard to distinguish whether the star formation in those clumps is triggered or pre-existing.

The physical properties statistics for both starless clumps and protostellar clumps are presented in Table 2. Starless clumps have lower temperature. And the average luminosity–mass ratio of starless clumps is less than 1, while that of protostellar clumps is about 24.5.

Table 1. Physical properties of JPS compact sources derived from SED fitting. The columns are as follows: (1)–(6): JPS source name, coordinates information, and source size come from Eden et al. (2017); (7) equivalent radius, calculated by $d\sqrt{A/\pi}$, where $d = 7.07$ kpc and A is the area of the source; (8)–(14): dust temperature, column density, mass surface density, mass, luminosity, and luminosity–mass ratio obtained from the SED fitting result.

ID	Name	ℓ_{peak}	b_{peak}	maj	min	PA	r_{eq}	T_{dust}	N_{H_2}	n_{H_2}	Σ_{mass}	Mass	Luminosity	*L*/*M* ratio
				(arcsec)	(arcsec)	(deg)	(pc)	(K)	(10^{22} cm^{-2})	(10^4 cm^{-3})	(g cm^{-2})	($M_\odot$)	($L_\odot$)	($L_\odot/M_\odot$)
	(1)	(2)	(3)	(4)	(5)	(6)	(7)	(8)	(9)	(10)	(11)	(12)	(13)	(14)
1	JPSG031.925+00.083	31.925	0.083	17	7	185	0.37	16.53	2.50	2.56	0.12	3.88e+02	4.35e+02	1.12
2	JPSG031.929+00.056	31.929	0.056	12	8	151	0.34	18.23	1.71	2.42	0.08	2.66e+02	4.35e+02	1.64
3	JPSG031.933+00.090	31.933	0.090	17	8	244	0.40	16.38	2.62	2.19	0.12	4.06e+02	4.94e+02	1.22
4	JPSG031.945+00.076	31.945	0.076	17	12	211	0.49	14.99	3.92	2.97	0.18	1.01e+03	6.45e+02	0.64
5	JPSG031.951+00.071	31.951	0.071	10	5	148	0.24	15.31	3.60	9.01	0.17	3.72e+02	1.66e+02	0.45
6	JPSG031.961+00.066	31.961	0.066	19	11	97	0.50	15.58	3.49	3.07	0.16	1.08e+03	7.45e+02	0.69
7	JPSG031.965+00.062	31.965	0.062	9	6	116	0.25	15.60	3.53	7.87	0.17	3.64e+02	1.95e+02	0.54
8	JPSG031.970+00.060	31.970	0.060	14	10	255	0.41	15.67	3.43	4.59	0.16	8.87e+02	5.08e+02	0.57
9	JPSG031.984+00.065	31.984	0.065	14	12	231	0.44	15.36	4.32	3.51	0.20	8.93e+02	6.76e+02	0.76
10	JPSG031.991+00.067	31.991	0.067	12	6	260	0.29	15.15	4.78	6.93	0.22	4.94e+02	2.94e+02	0.60
11	JPSG031.997+00.067	31.997	0.067	10	10	110	0.34	15.12	4.94	4.37	0.23	5.11e+02	4.17e+02	0.82
12	JPSG032.012+00.057	32.012	0.057	17	13	205	0.51	14.00	10.85	8.76	0.51	3.36e+03	1.23e+03	0.37
13	JPSG032.019+00.065	32.019	0.065	22	16	144	0.64	14.92	10.02	7.39	0.47	5.69e+03	2.64e+03	0.46
14	JPSG032.027+00.059	32.027	0.059	20	11	95	0.51	15.39	10.89	8.86	0.51	3.37e+03	2.13e+03	0.63
15	JPSG032.037+00.056	32.037	0.056	17	10	262	0.45	17.59	11.49	13.76	0.54	3.56e+03	3.75e+03	1.05
16	JPSG032.044+00.059	32.044	0.059	16	13	109	0.49	22.32	8.08	7.15	0.38	2.50e+03	1.33e+04	5.30
17	JPSG032.062+00.071	32.062	0.071	10	6	132	0.27	19.62	2.03	3.86	0.09	2.09e+02	4.96e+02	2.37
18	JPSG032.087+00.076	32.087	0.076	21	7	237	0.42	20.53	1.55	1.54	0.07	3.20e+02	1.22e+03	3.83
19	JPSG032.097+00.076	32.097	0.076	11	7	154	0.30	20.66	1.58	3.10	0.07	2.44e+02	6.78e+02	2.78
20	JPSG032.116+00.090	32.116	0.090	25	18	150	0.73	29.94	1.74	1.05	0.08	1.17e+03	3.92e+04	33.49
21	JPSG032.141+00.172	32.141	0.172	14	8	240	0.36	18.85	1.67	2.50	0.08	3.46e+02	6.06e+02	1.75
22	JPSG032.150+00.133	32.150	0.133	22	17	262	0.66	22.69	4.62	3.11	0.22	2.62e+03	1.59e+04	6.07
23	JPSG032.152+00.122	32.152	0.122	16	12	125	0.47	20.09	3.42	2.84	0.16	8.83e+02	3.01e+03	3.41
24	JPSG032.160+00.113	32.160	0.113	17	11	209	0.47	19.73	2.00	1.73	0.09	5.15e+02	1.57e+03	3.05
25	JPSG032.164+00.171	32.164	0.171	9	6	216	0.25	17.86	2.12	2.37	0.10	1.10e+02	2.67e+02	2.43
26	JPSG032.170+00.135	32.170	0.135	9	6	163	0.25	19.23	2.19	2.44	0.10	1.13e+02	4.27e+02	3.77
27	JPSG032.179+00.137	32.179	0.137	11	5	147	0.25	18.54	1.97	2.13	0.09	1.02e+02	3.16e+02	3.10

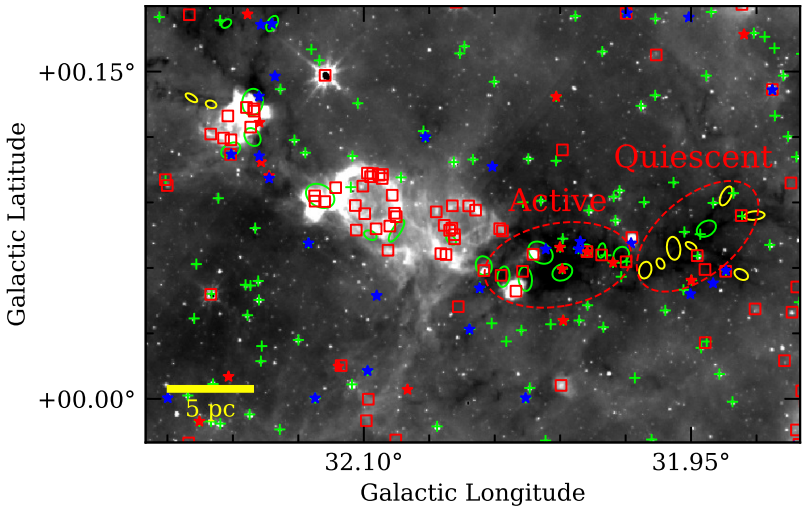

Figure 5. The distributions of Class I YSOs (red stars), Class II YSOs (blue stars), 24 μm point sources (green crosses), and 70 μm point sources (red squares). The background image is *Spitzer* 8 μm continuum map. Starless clumps are shown in yellow ellipses and protostellar clumps are shown in green ellipses. The IRDC can be divided into active part and quiescent part, both of them are marked by red dash ellipses.

Table 2. Physical properties statistics of JPS clumps.

	r_{eq}	T_{dust}	N_{H_2}	n_{H_2}	Σ_{mass}	Mass	Luminosity	L/M ratio
	(pc)	(K)	(10^{22} cm^{-2})	(10^4 cm^{-3})	(g cm^{-2})	($M_\odot$)	($L_\odot$)	($L_\odot/M_\odot$)
				Starless clumps				
Min	0.24	10.8	1.43	1.31	0.07	6.51e+01	3.53e+01	0.14
Max	0.5	18.1	6.22	6.24	0.29	6.11e+02	2.32e+02	3.07
Median	0.34	12.72	2.86	1.73	0.13	2.57e+02	1.03e+02	0.37
Mean	0.33	13.48	3.12	2.42	0.15	2.67e+02	1.17e+02	0.80
				Protostellar clumps				
Min	0.25	11.68	0.64	0.38	0.03	4.8e+01	7.16e+01	0.22
Max	0.73	38.18	11.6	6.31	0.54	1.99e+03	1.30e+05	233.60
Median	0.46	17.05	2.875	1.66	0.14	4.66e+02	7.88e+02	2.00
Mean	0.45	19.64	3.98	2.14	0.19	6.71e+02	1.42e+04	24.47

4 DISCUSSION

4.1 Dynamical structure of IRDC G31.97+0.07

4.1.1 Column density probability distribution functions

The column density probability distribution function (PDF) is defined as the probability of finding gas within a bin [N, N+dN]. PDFs are a useful tool to study the properties of ISM (Padoan, Jones & Nordlund 1997b; Burkhart et al. 2013), the core and stellar initial mass function (IMF) (Padoan & Nordlund 2002; Elmegreen 2011; Veltchev, Klessen & Clark 2011; Donkov, Veltchev & Klessen 2012), and the SFR (Krumholz & McKee 2005; Padoan & Nordlund 2011; Federrath & Klessen 2012).

Theoretical work and simulations (Vazquez-Semadeni 1994; Padoan, Nordlund & Jones 1997a; Kritsuk et al. 2007; Federrath, Klessen & Schmidt 2008; Vázquez-Semadeni et al. 2008; Federrath et al. 2010) show that the density PDF of the gas dominated by isothermal supersonic turbulence is approximated well by a lognormal form. Deviations from the lognormal shape, which are mostly in the form of power-law tails, are present in simulations when compressible turbulence and/or self-gravity are considered (Passot & Vázquez-Semadeni 1998; Klessen, Heitsch & Mac Low 2000; Kritsuk, Norman & Wagner 2011; Federrath & Klessen 2013).

As many previous studies did, due to the huge range of column densities, we switch to a logarithmic scale $\eta = \ln(N_{H_2})/\langle N_{H_2}\rangle$, where N_{H_2} is the column density and $\langle N_{H_2}\rangle$ is the average column density of the cloud. So, the form of the PDF at low-densities that is characterized by being lognormal can be written as

$$p(\eta) = \frac{p_0}{\sqrt{2\pi\sigma_0^2}} \exp\left(\frac{-(\eta-\eta_0)^2}{2\sigma_1^2}\right), \quad (10)$$

where η_0, p_0, and σ_0 are the peak value, integral probability, and standard deviation. And the power-law tail at high densities:

$$p(\eta) \propto N_{H_2}^m, \quad (11)$$

The models including self-gravity (Klessen et al. 2000; Kritsuk et al. 2011; Federrath & Klessen 2013) indicate that the exponent m can respond to an equivalent spherical density profile of exponent α: $\rho(r) \propto r^{-\alpha}$, where $\alpha = 1 - 2/m$. Those work also suggest that α of a spherical self-gravitating cloud value between 1.5 and 2 ($-4 < m < -2$), which is supported by observational study of several IRDCs (Schneider et al. 2015; Yuan et al. 2018).

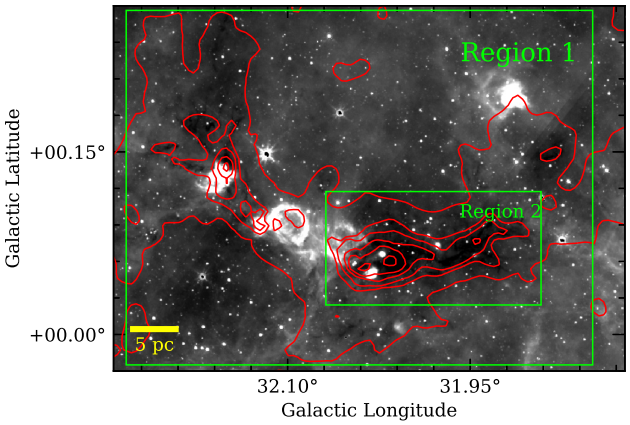

Figure 6. The green rectangles indicates the regions used for PDFs. The background image is *Spitzer* 8 μm continuum overlaid by the contour of the column density map derived from pixel-to-pixel SED fitting (see in Section 3.3). Region 1: the whole filamentary structure; Region 2: IRDC G31.97+0.07.

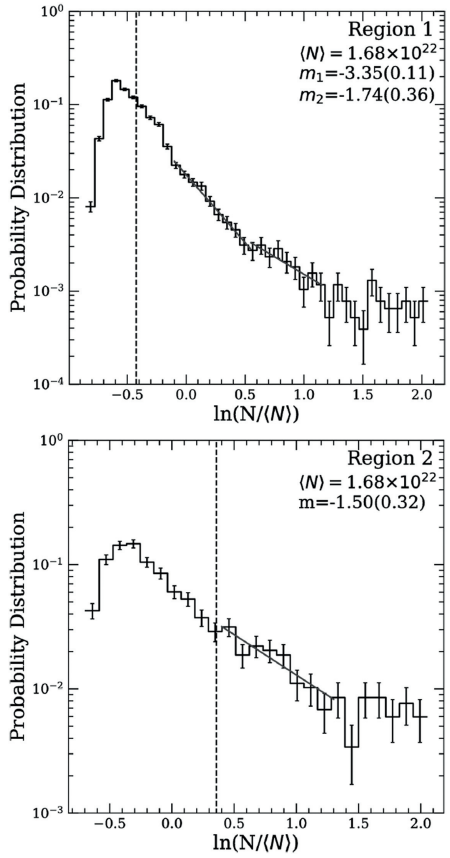

Figure 7. Column density PDFs of the two regions are shown in Fig. 6. The error bars are calculated from Poisson noise in each bin. The black dashed line corresponds to the last closed contour that is regarded as the completeness limit. The power-law tail at high-column densities is shown by the violet line.

In this work, we determined the PDFs in two regions that are shown in Fig. 6. Region 1 covers the whole filamentary structure including the H II regions and the IRDC. Region 2 only contains the IRDC in the west. Fig. 7 shows the PDFs of those two regions. The error bars show the statistical Poisson error in each bin. The average column density $\langle N \rangle = 1.68 \times 10^{22}\,\mathrm{cm}^{-2}$. The black dashed line corresponds to the last closed contour that is regarded as the completeness limit (Lombardi, Alves & Lada 2015; Ossenkopf-Okada et al. 2016; Alves, Lombardi & Lada 2017). The completeness limit is −0.42 for Region 1 and 0.36 for Region 2.

For the part above the completeness limit, neither PDFs of Region 1 nor Region 2 represent lognormal well. Thus, we only discuss their power-law tails. One can easily notice that the PDF of Region 1 can be described by two power laws with demarcation between 0.5 and 0.6. The slope m is −3.35(0.11) for the power law at lower column densities and −1.74(0.36) for the power law at higher column densities. We fit the power law for the PDF of Region 2 from 0.5 to 1.2, the slope m is −1.50(0.32). Comparing the PDFs of Region 1 and Region 2, we suggest that flat power law at higher column densities is mainly contributed from the IRDC. That means more dense gas accumulates in the IRDC. The power law of the PDF of the IRDC is flatter than theoretical prediction, which implies that this region may be compressed by the adjacent H II region at the south west according Fig. 1. This suggests that when the ionized-gas pressure is higher than the turbulent ram pressure the ionized-gas would compress the material around the ionizing source, as shown in the numerical simulation of Tremblin et al. (2012). And the ionization compression can also play a role at high column densities that are expected to be gravity dominant, as found by Tremblin et al. (2014) in *Rosette* nebula.

4.1.2 *Investigating of the fragmentation of the IRDC*

The model of a self-gravitating fluid cylinder can be used to describe a filamentary IRDC. The theoretical work describing the fragmentation of fluid cylinders due to the 'sausage' instability has been established decades earlier (e.g. Chandrasekhar & Fermi 1953; Nagasawa 1987; Inutsuka & Miyama 1992; Tomisaka 1995). The theory predicts that the filament should fragment into multiple cores with quasi-regular spacing that has been observed in several filamentary molecular clouds (e.g. Jackson et al. 2010; Wang et al. 2014; Henshaw et al. 2016). The characteristic spacing between cores corresponds to the wavelength of the fastest-growing unstable mode of the fluid instability.

For an incompressible fluid cylinder, the fragment spacing is $\lambda = 11R$, where R is the radius of the cylinder, given by Chandrasekhar & Fermi (1953). And for an infinite isothermal gas cylinder (Nagasawa 1987):

$$\lambda = 22H = \frac{22c_\mathrm{s}}{(4\pi G\rho)^{1/2}}, \tag{12}$$

where H is the isothermal scale height, c_s is the sound speed, G is the gravitational constant, and ρ is the gas density of the filament. For a finite isothermal cylinder embedded in external uniform medium, the fragments spacing depend on the ratio of cylinder radius R and isothermal scale height H. If $R \gg H$, $\lambda = 22H$, and if $R \ll H$, $\lambda = 11R$.

For IRDC G31.97+0.07, the sound speed $c_\mathrm{s} = [(k_\mathrm{B}T)/(\mu_\mathrm{p} m_\mathrm{H})]^{1/2} \approx 0.22\,\mathrm{km\,s}^{-1}$, where k_B is the Boltzmann constant, $T \approx 16\,\mathrm{K}$ is the mean temperature derived from SED fitting, $\mu_\mathrm{p} = 2.33$ is the mean molecular weight per free particle, and m_H is the mass of atomic hydrogen. Thus, the isothermal scale height $H = c_\mathrm{s}/(4\pi G\rho)^{1/2} \approx 0.015\,\mathrm{pc}$, where $\rho = \mu_{\mathrm{H}_2} m_\mathrm{H} n_{\mathrm{H}_2}$ and $n_{\mathrm{H}_2} \sim 5.6 \times 10^4\,\mathrm{cm}^{-3}$. Since the radius R of the filament (∼0.01° or ∼1.2 pc at 7.07 kpc) is much larger than the isothermal scale height H, under the isothermal and thermally supported assumption, the predicted theoretical fragment spacing is $\lambda = 22H = 0.33\,\mathrm{pc}$.

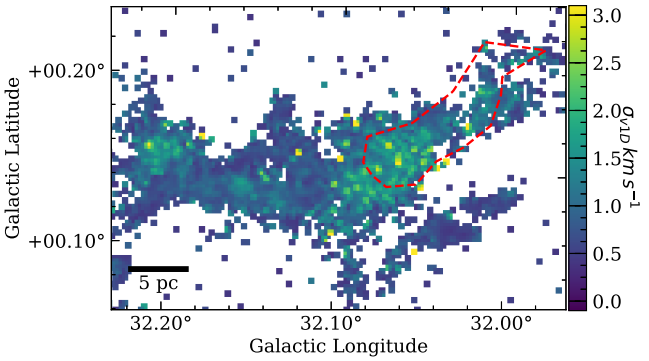

Figure 8. The map of ^{13}CO (3–2) line velocity dispersion. σ_{v1D} of each pixel is derived from Gaussian fitting of the ^{13}CO (3–2) line observed by JCMT in the velocity interval between 90 and 100 km s^{-1}. The red dashed polygon shows the position of the IRDC.

The spacing of 15 clumps located in the IRDC ranges from 0.66 to 1.31 pc, with an average of 0.97 pc and a median of 0.94 pc. This agrees with the distribution of the clump spacing and is roughly symmetrical, and five clumps have spacing value in the interval of [0.89, 0.98] pc. Although the discussion of the clump spacing distribution is difficult for such a small sample, we can still consider that the clumps have a characteristic spacing of 0.97 ± 0.03 pc and use it in the following discussion.

As we consider the effect of inclination, assuming the inclination angle $i = 30°$, the observational fragments spacing should be corrected by $\lambda_{obs,i} = \lambda_{obs}/\cos(i) = 1.12$ pc, which is much larger than the theoretical predicted 0.33 pc. This discrepancy may be caused by the fact that the IRDC is turbulence and not thermal-pressure dominated.

When considering turbulence, the sound speed c_s in equation (12) can be replaced by total velocity dispersion σ_v (Fiege & Pudritz 2000). To derive the total velocity dispersion of the IRDC, we fitted the spectrum of ^{13}CO (3–2), observed by JCMT in the velocity interval between 90 and 100 km s^{-1}, pixel-by-pixel with a Gaussian profile. The result is shown in Fig. 8. The velocity dispersion σ_v is given by Fuller & Myers (1992):

$$\sigma_v = \sqrt{\sigma^2_{^{13}\mathrm{CO}} + k_\mathrm{B}T\left(\frac{1}{\mu_{\mathrm{H}_2} m_\mathrm{H}} - \frac{1}{m_{^{13}\mathrm{CO}}}\right)}, \quad (13)$$

where $\sigma_{^{13}\mathrm{CO}}$ is the ^{13}CO line velocity dispersion derived from Gaussian fitting, $m_{^{13}\mathrm{CO}} = 29 m_\mathrm{H}$ is the mass of ^{13}CO. For the IRDC, the average ^{13}CO line velocity dispersion $\sigma_{^{13}\mathrm{CO}} \approx 1.09 \pm 0.45$ km s^{-1}; hence, the total velocity dispersion $\sigma_v \approx 1.10 \pm 0.45$ km s^{-1}. Replacing c_s in equation (12) by σ_v, the expected fragment spacing is $\lambda \approx 1.7 \pm 0.7$ pc, about 1.5 times larger than the observed value but consistent with the error range.

Kainulainen et al. (2013) suggest that at the scale smaller than Jeans' length, the fragmentation more closely resembles Jeans' fragmentation. According to the spherical Jeans' instability, the clump separation is related to density via Jeans' length, $\lambda_\mathrm{J} = c_s(\pi/(G\rho))^{1/2}$. Here, the sound speed c_s is replaced by velocity dispersion σ_v, and we obtain $\lambda_\mathrm{J} = 0.48$ pc for the IRDC. That is smaller than all the observational clump spacing, which suggests that the IRDC fragmentation is roughly dominated by the collapse of the natal filament.

The previous discussion is based on the hydrostatic models, but actually, the filament may be non-equilibrium and fragmenting with accreting. Clarke, Whitworth & Hubber (2016) studied the fragmentation of non-equilibrium, accreting filaments and suggested that an age limit for a filament, which is fragmenting periodically could be estimated by measuring the average core separation distance λ (see also Williams et al. 2018):

$$\tau_\mathrm{age} \geq \tau_\mathrm{crit} \simeq \frac{\lambda}{2c_s}, \quad (14)$$

where sound speed c_s should be replaced by velocity dispersion σ_v. And τ_crit can also be related to the mass accretion rate $\dot{M}$:

$$\tau_\mathrm{crit} = \frac{\lambda}{2\sigma_v} = \frac{M_\mathrm{line,crit}}{\dot{M}}, \quad (15)$$

where $M_\mathrm{line,crit} = 2\sigma_v^2/G = 563\,\mathrm{M}_\odot\,\mathrm{pc}^{-1}$ in this work (G is the gravitational constant). Thus, we can derive $\dot{M}$ as $1.3 \times 10^3\,\mathrm{M}_\odot\,\mathrm{pc}^{-1}\,\mathrm{Myr}^{-1}$ (with $i = 0°$) or $1.1 \times 10^3\,\mathrm{M}_\odot\,\mathrm{pc}^{-1}\,\mathrm{Myr}^{-1}$ (with $i = 30°$). If assuming mass accretion rate remained constant during the filament evolution, we derive the age τ_age through

$$\tau_\mathrm{age} = \frac{M_\mathrm{line}}{\dot{M}}. \quad (16)$$

As the mass of the 11 pc long filament is about $7.8 \times 10^4\,\mathrm{M}_\odot$ (mentioned at Section 3.3). The age of filament τ_age is ∼5.5 Myr (with $i = 0°$) or ∼6.4 Myr (with $i = 30°$).

4.2 Properties of JPS clumps

4.2.1 CO line profiles of clumps

For each clumps, we extract ^{12}CO (3–2) spectra from COHRS, ^{13}CO (3–2) and C^{18}O (3–2) from CHIMPS. The spectra of all clumps are shown in the Appendix. Some clumps contain multiple velocity components, which makes our analysis difficult. The peak values of ^{13}CO (3–2) for some other clumps do not achieve 3σ threshold of main beam efficiency corrected CHIMPS data (∼2.4 K). Thus, in the following discussion, we only consider the strongest component of which the ^{13}CO (3–2) intensity must be higher than 3σ threshold for each clump, as some previous study did (Urquhart et al. 2007; Eden et al. 2012, 2013). There are 18 clumps that meet this requirement, 16 of which are protostellar and 2 are starless. And C^{18}O (3–2) emission higher than 2.4 K are detected in only 9 clumps.

According to radiative transfer, brightness temperature (T_r) can be expressed as

$$T_r = \frac{h\nu}{k}\left[\frac{1}{\exp(h\nu/kT_\mathrm{ex})} - \frac{1}{\exp(h\nu/kT_\mathrm{bg})}\right] \times (1 - \mathrm{e}^{-\tau})f, \quad (17)$$

where $T_\mathrm{bg} = 2.73$ K is the temperature of cosmic background radiation, and f which is the beam-filling factor can be consider to be 1 here. Under the LTE condition, the optical depths of CO and ^{13}CO can be obtain by

$$\frac{T_{r,\mathrm{CO}}}{T_{r,^{13}\mathrm{CO}}} \approx \frac{1 - \exp(-\tau_\mathrm{CO})}{1 - \exp(-\tau_{^{13}\mathrm{CO}})}, \quad (18)$$

where $\tau_\mathrm{CO}/\tau_{^{13}\mathrm{CO}} = [\mathrm{CO}]/[^{13}\mathrm{CO}] \approx 89$. According the equation, we obtain the optical depths of ^{13}CO, the results are listed in the Column 7 in the Table 3. The $\tau_{^{13}\mathrm{CO}}$ ranges from 0.33 to 1.05, so we can generally consider ^{13}CO (3–2) as optically thin.

The asymmetry of line profiles can be used to probe different dynamic features. Generally, blue profiles are caused by collapse or infall motion, and red profiles are linked to expansion or outflow motion (Mardones et al. 1997). To select clumps with blue or red profiles, we adopted the normalized criterion set by Mardones et al. (1997):

$$\delta_V = (V_\mathrm{thick} - V_\mathrm{thin})/\Delta V_\mathrm{thin}, \quad (19)$$

Table 3. Line profiles parameters of JPS clumps. Optically thick line: CO (3–2); Optically thin line: ^{13}CO (3–2). '*' labels the clumps of which C^{18}O (3–2) are used as optically thin lines in the following discussion; Column (2): evolutionary type of clumps (see in Section 3.4). Columns (3)–(9): parameters used in equation (19) to select blue/red profile. Coulmn (7): line profiles, BP: blue profile, RP: red profile. '**' labels the clumps which may be misclassified by multiple velocity components. Coulmn (11): infall velocities of the clumps with blue profiles, obtained from equation (20).

ID	Name	Type	$V_{\rm peak,\,thick}$ (km s^{-1})	$T_{r,\,\rm thick}$ (K)	$V_{\rm peak,\,thin}$ (km s^{-1})	$T_{r,\,\rm thin}$ (K)	$\tau_{^{13}\rm CO}$	FWHM$_{\rm thin}$ (km s^{-1})	δ_V	Profile (km s^{-1})	$V_{\rm in}$
	(1)	(2)	(3)	(4)	(5)	(6)	(7)	(8)	(9)	(10)	(11)
4	JPSG031.945+00.076	Protostellar	93.1	8.29	96.00	2.45	0.35	2.96	−0.98	BP	0.21
9	JPSG031.984+00.065	Protostellar	92.1	11.85	93.68	3.88	0.40	2.52	−0.63	BP**	
10	JPSG031.991+00.067	Protostellar	92.1	14.43	94.62	4.01	0.33	4.09	−0.62	BP	0.47
11	JPSG031.997+00.067	Protostellar	92.1	13.51	95.10	4.46	0.40	3.68	−0.82	BP	0.21
12	JPSG032.012+00.057	Protostellar	94.1	13.75	96.31	5.03	0.45	3.31	−0.67	BP**	
13	JPSG032.019+00.065	Protostellar	97.1	14.59	98.87	5.99	0.53	4.15	−0.43	BP**	
14	JPSG032.027+00.059	Protostellar	93.1	19.47	94.73	6.34	0.39	3.80	−0.43	BP**	
15	JPSG032.037+00.056	Protostellar	93.1	17.54	94.49	8.08	0.62	3.26	−0.43	BP**	
16	JPSG032.044+00.059	Protostellar	92.1	16.45	94.82	10.36	0.99	3.45	−0.79	BP	0.13
17	JPSG032.062+00.071	Protostellar	95.1	13.42	95.42	6.32	0.63	2.44	−0.13	–	
18	JPSG032.087+00.076	Protostellar	97.1	14.25	97.01	8.57	0.92	2.00	0.05	–	
19	JPSG032.097+00.076	Protostellar	94.1	10.80	95.98	7.04	1.05	2.58	−0.73	BP	0.44
20	JPSG032.116+00.090*	Protostellar	97.1	22.46	96.18	6.40	0.96	2.65	0.35	RP	
22	JPSG032.150+00.133*	Protostellar	96.1	19.77	94.45	3.35	0.72	3.94	0.42	RP	
23	JPSG032.152+00.122	Protostellar	96.1	15.60	96.08	8.56	0.80	2.32	0.01	–	
24	JPSG032.160+00.113	Protostellar	96.1	14.88	96.46	7.46	0.70	1.82	−0.20	–	
26	JPSG032.170+00.135	Starless	95.1	8.72	94.83	3.61	0.53	1.94	0.14	–	
27	JPSG032.179+00.137	Starless	95.1	5.92	94.94	2.70	0.61	1.67	0.09	–	

where $V_{\rm thick}$ is the velocity of the optically thick line [i.e. CO (3–2) in our discussion] at peak value, $V_{\rm thin}$ and $\Delta V_{\rm thin}$ are the systemic velocity and line width of the optically thin line, i.e. ^{13}CO (3–2). For the clumps that may contain multiple components, their $\Delta V_{\rm thin}$ are measured by Gaussian fitting for the strongest component. If $\delta_V < -0.25$, the line profile is considered a blue profile, and if $\delta_V > 0.25$, the line profile is considered to be red. For Clumps 20 and 22, comparing profiles of ^{13}CO and C^{18}O (3–2), we find that their ^{13}CO (3–2) might be self-absorbed. As their C^{18}O (3–2) emissions are strong enough, we choose their C^{18}O (3–2) as optically thin lines in this part of discussion.

Our classification is shown in Table 3. For the 18 clumps, we find that 10 clumps show blue profiles, and 2 clumps show red profiles. After visual inspection we exclude five clumps as they may be misclassfied by multiple velocity components, and they are marked in Table 3.

According to Myers et al. (1996), we can estimate infall velocities of the clumps with blue profiles:

$$V_{\rm in} \approx \frac{\sigma_v}{v_{\rm red} - v_{\rm blue}} \ln\left(\frac{1 + {\rm e}T_{\rm BD}/T_{\rm D}}{1 + {\rm e}T_{\rm RD}/T_{\rm D}}\right), \quad (20)$$

where $T_{\rm D}$ is the brightness temperature of the dip of the optically thick line. $T_{\rm BD}(T_{\rm RD})$ is the height of the blue (red) peak above the peak. The velocity dispersion σ_v is obtained from the FWHM of an optically thin line.

The calculation results of five clumps with blue profiles are listed in Table 3. The infall velocities of them range from 0.13 to 0.47 km s^{-1}, with a mean value of 0.31 km s^{-1}.

4.2.2 The stability of clumps

Using the physical properties we obtain in the previous analysis, we can study the stability of JPS clumps, i.e. whether they are susceptible to gravitational collapse or expansion in the absence of pressure confinement.

First, we consider the thermal Jeans instability,

$$M_{\rm J} = \frac{\pi^{5/2} c_{\rm s}^3}{6\sqrt{G^3\rho}}, \quad (21)$$

$$\text{and } \lambda_{\rm J} = c_{\rm s}\left(\frac{\pi}{G\rho}\right)^{1/2}, \quad (22)$$

where $M_{\rm J}$ and $\lambda_{\rm J}$ are the Jeans mass and Jeans length, $c_{\rm s}$ is the sound speed, and $\rho = \mu_{\rm H_2} m_{\rm H} n_{\rm H_2}$ is the density. When clumps are both thermally and turbulently supported, the sound speed $c_{\rm s}$ is replaced by the velocity dispersion σ_v.

Another important parameter to estimate the stability of clumps is virial parameter $\alpha_{\rm vir}$:

$$\alpha_{\rm vir} \equiv \frac{M_{\rm vir}}{M_{\rm clump}} = \frac{5\sigma_v^2 R_{\rm eq}}{G M_{\rm clump}}, \quad (23)$$

similarly σ_v is the velocity dispersion contributed from both thermal motions and turbulence, $R_{\rm eq}$ is the equivalent radius of the clump and $M_{\rm clump}$ is the clump mass. According to McKee & Holliman (1999) and Kauffmann, Pillai & Goldsmith (2013), in a non-magnetized cloud, if $\alpha_{\rm vir} < 2$, the cloud is gravitationally bound and will tend to collapse, otherwise, it may expand by lack of pressure confinement.

The calculation results are shown in Table 4. In our calculation, we adopt the velocity dispersion derived from the width of optically thin line, which have been obtained in Section 4.2.1. Only one clump has $\alpha_{\rm vir} > 2$, suggesting that most the clumps of the filament are gravitationally bound and likely to collapse. There are 12 clumps with $\lambda_{\rm Jeans} < 2R_{\rm eq}$, indicating that they are likely to split into smaller fragments while collapsing. In addition, we have to point out that the $\alpha_{\rm vir}$ of three clumps (Clumps 10, 11, and 19) with blue profiles may be overestimate, as the line may be broadened by gas infall motion.

Table 4. The gas dynamical properties and viral parameters of JPS clumps derived from ^{13}CO (3–2) data. Column (3): The velocity dispersion which is derived from the optically thin line width in Table 3. Columns (5)–(8): Viral mass, Jeans mass, Jeans length, and viral parameter calculated from velocity dispersion.

ID	Name	$R_{\rm eq}$ (pc)	σ_v (km s^{-1})	$M_{\rm clump}$ (M$_\odot$)	$M_{\rm vir}$ (M$_\odot$)	$M_{\rm Jeans}$ (M$_\odot$)	$\lambda_{\rm Jeans}$ (pc)	$\alpha_{\rm vir}$
	(1)	(2)	(3)	(4)	(5)	(6)	(7)	(8)
4	JPSG031.945+00.076	0.49	1.27	1.01e+03	9.24e+02	4.71e+02	0.76	0.92
9	JPSG031.984+00.065	0.44	1.09	8.93e+02	6.07e+02	2.71e+02	0.60	0.68
10	JPSG031.991+00.067	0.29	1.75	4.94e+02	1.03e+03	7.95e+02	0.68	2.08
11	JPSG031.997+00.067	0.34	1.57	5.11e+02	9.79e+02	7.32e+02	0.77	1.92
12	JPSG032.012+00.057	0.51	1.42	3.36e+03	1.19e+03	3.80e+02	0.49	0.36
13	JPSG032.019+00.065	0.64	1.77	5.69e+03	2.34e+03	8.08e+02	0.67	0.41
14	JPSG032.027+00.059	0.51	1.63	3.37e+03	1.57e+03	5.69e+02	0.56	0.47
15	JPSG032.037+00.056	0.45	1.40	3.56e+03	1.03e+03	2.92e+02	0.39	0.29
16	JPSG032.044+00.059	0.49	1.49	2.50e+03	1.26e+03	4.82e+02	0.57	0.50
17	JPSG032.062+00.071	0.27	1.06	2.09e+02	3.52e+02	2.38e+02	0.55	1.68
18	JPSG032.087+00.076	0.42	0.88	3.20e+02	3.80e+02	2.18e+02	0.73	1.19
19	JPSG032.097+00.076	0.30	1.12	2.44e+02	4.36e+02	3.12e+02	0.65	1.79
20	JPSG032.116+00.090	0.73	1.38	1.17e+03	1.61e+03	1.00e+03	1.38	1.38
22	JPSG032.150+00.133	0.66	1.77	2.62e+03	2.40e+03	1.23e+03	1.03	0.91
23	JPSG032.152+00.122	0.47	1.01	8.83e+02	5.59e+02	2.41e+02	0.62	0.63
24	JPSG032.160+00.113	0.47	0.81	5.15e+02	3.57e+02	1.58e+02	0.63	0.69
26	JPSG032.170+00.135	0.25	0.85	1.13e+02	2.12e+02	1.56e+02	0.56	1.87
27	JPSG032.179+00.137	0.25	0.74	1.02e+02	1.61e+02	1.11e+02	0.52	1.58

4.2.3 *The evolutionary stage of clumps*

The luminosity–mass diagram is an effective tool to infer the evolutionary phases of the clumps. Saraceno et al. (1996) used this diagram to describe the evolutionary stages of low-mass objects, and Molinari et al. (2008) used it extendedly for the study of evolutionary tracks of high-mass regions.

The luminosity–mass diagram of the clumps is shown in Fig. 9 with starless clumps denoted by red crosses and protostellar clumps by blue stars. The diagram is also superimposed with the evolutionary paths from Molinari et al. (2008) for cores with different initial envelope mass. The paths follow the two-phase model of McKee & Tan (2003). According to the model, in the first phase, when a clump gravitationally collapses, the mass slightly decreases due to accretion and molecular outflow, while its luminosity significantly increases, and the object moves along an almost vertical path in the $L_{\rm clump}-M_{\rm clump}$ diagram. At the end of the first phase, the object is surrounded by an H II region and begins to expel surrounding material through radiation and outflow. In the second phase, the object follows a horizontal track with a nearly constant luminosity and decreasing mass. Although these evolutionary tracks are initially modelled for single cores and some high-mass clumps may contain multiple cores in different evolutionary stages, the $L_{\rm clump}-M_{\rm clump}$ diagram has been used in the past to discuss the evolutionary stages of both low-mass and high-mass clumps (Hennemann et al. 2010; Elia et al. 2010; Traficante et al. 2015; Yuan et al. 2017).

The black solid and dashed lines in Fig. 9 show the best log–log fit for Class I and Class 0 objects. We only find two protostellar clumps located between these two lines, and one protostellar clump lies above the log–log fit of Class I objects. Molinari et al. (2016b) suggest that $L_{\rm clump}/M_{\rm clump} \leq 1\,{\rm L}_\odot/{\rm M}_\odot$ is the characteristic for starless clumps, and we show this criterion by the green dashed line in Fig. 9. However, Traficante et al. (2015) identify 667 starless clumps in IRDCs from *Herschel* data and suggest the mean $L_{\rm clump}/M_{\rm clump} \simeq 1.1$ for the starless clump distribution. Generally, the starless clumps in our sample are distributed along or under the green dashed line, with mean $L_{\rm clump}/M_{\rm clump} \simeq 1.4$, which indicates that these clumps are still in the very early stages of their evolution. We also find seven protostellar clumps with $L_{\rm clump}/M_{\rm clump} < 1$. We suggest that they may be misclassified due to foreground mid-IR point sources. Another probable explanation is that they do contain YSOs, but the rest of the clump is still cold and quiescent. Thus, on average, their *L*–*M* ratios still keep low.

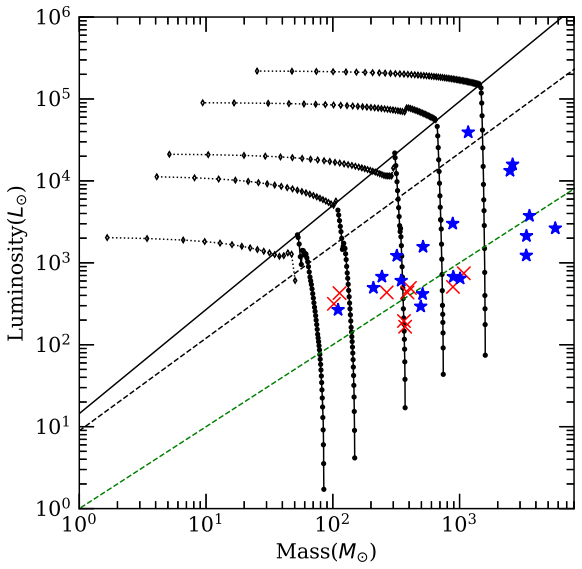

Figure 9. Luminosity–mass diagram for the clumps superimposed with the model of Molinari et al. (2008, black tracks with symbols). Starless clumps are shown by red crosses, and protostellar clumps by blue stars. The different tracks (left to right) are for different initial clump masses of 80, 140, 350, 700, and 2000 M$_\odot$. The black solid and dashed lines are the best log–log fit for Class I and Class 0 sources extrapolated in the high-mass regime by Molinari et al. (2008). The green dashed line shows the characteristic of $L_{\rm clump}/M_{\rm clump} \leq 1\,{\rm L}_\odot/{\rm M}_\odot$ suggested by Molinari et al. (2016b) for starless clumps.

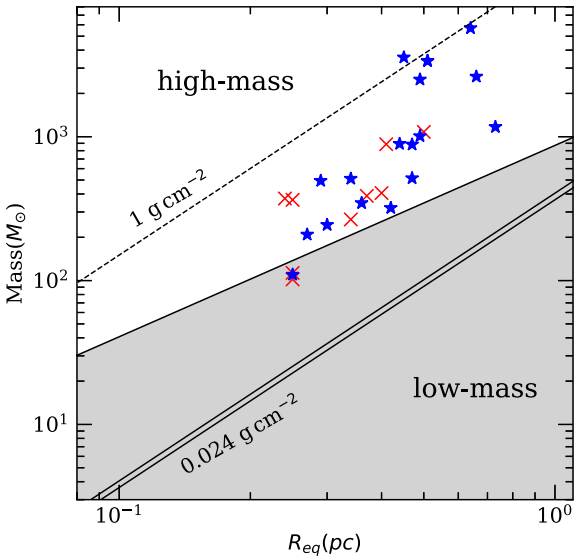

Figure 10. Clump mass as a function of equivalent radius for protostellar clumps (blue stars) and starless clumps (red crosses). The unshaded area delimits the region of high-mass star formation. The threshold is $M \geq 870\,M_\odot (r/\mathrm{pc})^{1.33}$ adopted from Kauffmann & Pillai (2010). Lower solid lines represent surface density thresholds for 'efficient' star formation of $116\,M_\odot\,\mathrm{pc}^{-2}$ ($\sim$0.024 g cm^{-2}) (Lada et al. 2010) and $129\,M_\odot\,\mathrm{pc}^{-2}$ ($\sim$0.027 g cm^{-2}) (Heiderman et al. 2010). The upper dashed line shows the criterion of 1 g cm^{-2} for high-mass star formation given by Krumholz & McKee (2008).

4.2.4 *High-mass star-forming regions*

To assess the potential of clumps to form massive stars, we have to consider their sizes and masses. Fig. 10 shows the mass versus equivalent radius diagram on which starless clumps are shown by red crosses and protostellar clumps by blue stars. All the JPS clumps satisfy the threshold for 'efficient' star formation of $116\,M_\odot\,\mathrm{pc}^{-2}$ ($\sim$0.024 g cm^{-2}) given by Lada, Lombardi & Alves (2010) or $129\,M_\odot\,\mathrm{pc}^{-2}$ ($\sim$0.027 g cm^{-2}), given by Heiderman et al. (2010). The thresholds are shown as the lower solid lines in Fig. 10. That means all of the clumps including starless clumps have sufficient material to form stars.

According to observations of nearby clouds, Kauffmann & Pillai (2010) give a more restrictive massive-star formation criterion of $M \geq 870\,M_\odot (r/\mathrm{pc})^{1.33}$. Only four clumps do not meet the criterion of massive-star formation, thus most clumps can potentially form high-mass stars. Six of the clumps above the threshold are starless clumps, so they are good candidates for studying massive star-forming regions in a very early evolutionary stage.

Moreover, mass surface density Σ_{mass} is another useful parameter to identify whether clumps have sufficient mass to form massive stars. Krumholz & McKee (2008) suggest that high-mass star formation requires a mass surface density larger than 1 g cm^{-2} to prevent fragmentation into low-mass cores through radiative feedback. Only one clump meets this criterion; however, this threshold is relatively uncertain, and it does not consider magnetic fields, which may play a significant role in preventing fragmentation. In addition, massive clumps and cores with Σ less than 1 g cm^{-2} are reported in some observations (e.g. Butler & Tan 2012; Tan et al. 2013).

5 SUMMARY

We present multiple infrared, sub-millimetre continuum and CO isotope rotation-line observations towards IRDC G31.97+0.07 on a large scale. From the continuum and spectral data, we get the dust temperature, column density, excitation temperature, and velocity dispersion of this region. The main results of this work are summarized as follows:

1. The dust temperature and molecular-hydrogen column density maps are derived from fitting the SED of the *Herschel* data pixel by pixel, using a grey-body model. The dust temperature of the IRDC is lower than the active star-formation region that contains UC H II regions and IR bubbles, while the column density of the IRDC is higher. The total mass is about $2.5 \times 10^5\,M_\odot$ for the whole filamentary structure and is about $7.8 \times 10^4\,M_\odot$ for the IRDC, based on the results.

2. From the column density map derived from SED fitting, we produce column density PDFs towards two regions – Region 1: the whole filamentary structure; Region 2: the IRDC. The PDFs of both Regions 1 and 2 mainly show power-law tails at the part above the completeness limit, suggesting that this region is gravity dominant.

Compared to other part, the power-law slope of the PDF of Region 2 is flatter, suggesting that more dense gas accumulates in the IRDC. For the PDF of Region 2, the power-law slope $m = -1.50(0.32)$ is flatter than the prediction of a spherical self-gravitating cloud model ($-4 < \mathrm{m} < -2$), which implies that this region may be compressed by the adjacent H II region.

3. The theory of self-gravitating, hydrostatic cylinders shows that the filament would fragment into cores with a roughly constant spacing caused by the 'sausage' instability. In this work, we derive the mean velocity dispersion by fitting the FWHM of the optically thin line, i.e. ^{13}CO (3–2). Taking the average velocity dispersion $\sigma_v \sim 1.1\,\mathrm{km\,s^{-1}}$, number density $n_{\mathrm{H_2}} \sim 2.2 \times 10^4\,\mathrm{cm^{-3}}$ and inclination angle $i = 30^\circ$, we find the mean observed fragment spacing ($\sim$1.12 pc) is about 1.5 times smaller than the prediction of the theoretical model ($\sim$1.7 pc).

Using another non-equilibrium, accreting model (Clarke et al. 2016), we estimate the age of the IRDC, which is about 6.4 Myr when $i = 30^\circ$.

4. There are 27 clumps that are identified from JPS 850 μm continuum located in the filamentary structure. Using the GLIMPSE point-source catalogue and the identification of the YSOs in the previous study, we get distributions of Class I and Class II YSOs. We classify them into two groups: protostellar clumps, which are associated with any YSOs, 24 or 70 μm point sources; and starless clumps that are not. We identify 9 starless clumps and 18 protostellar clumps. We derive physical properties of all the clumps from SED fitting. Compared to protostellar clumps, starless clumps have lower temperature and luminosity–mass ratios.

5. Spectral analysis are performed for 18 clumps with relatively strong ^{13}CO (3–2) emission. Using the optically thick line (i.e. ^{12}CO) and the optically thin (i.e. ^{13}CO or C^{18}O) spectra simultaneously, we identify 10 clumps with blue profiles asymmetry, while five of them may be misclassified by multiple velocity components. Blue profiles indicate infall motion. We obtain the average infall velocity of the clumps with blue profiles, which is about $0.31\,\mathrm{km\,s^{-1}}$.

We also calculate the virial parameters of all the 18 clumps to investigate their stabilities. Only one clumps has $\alpha_{\mathrm{vir}} > 2$, suggesting that most clumps are gravitationally bound and tend to collapse.

6. All of the 27 JPS clumps fulfil the 'efficient' star-formation threshold, thus they have sufficient mass to form stars. 23 clumps

(∼85 per cent) are above the threshold for high-mass star formation proposed by Kauffmann & Pillai (2010), and 6 of them are starless clumps. According to the luminosity–mass diagram, all the starless clumps in our sample are in very early evolutionary stages. Hence, those 6 starless clumps are good candidates for studying high-mass star-forming regions in very early evolutionary stage.

ACKNOWLEDGEMENTS

Chenlin Zhou, Ming Zhu and Lixia Yuan are supported by the China Ministry of Science and Technology under the State R&D Program (2017YFA0402600) and by the NSFC grant no. U1531246, 11503035, and also supported by the Open Project Program of the Key Laboratory of FAST, NAOC, Chinese Academy of Sciences. JHY is partly supported by the Young Researcher Grant of National Astronomical Observatories, Chinese Academy of Sciences.

The JCMT has historically been operated by the Joint Astronomy Centre on behalf of the Science and Technology Facilities Council of the United Kingdom, the National Research Council of Canada and the Netherlands Organisation for Scientific Research. JCMT continuum data were obtained by SCUBA-2. Additional funds for the construction of SCUBA-2 were provided by the Canada Foundation for Innovation. This work made use of data from the *Spitzer Space Telescope*, which is operated by the Jet Propulsion Laboratory, California Institute of Technology under a contract with NASA. This work also used data from Hi-GAL which is one of key projects of *Herschel* spacecraft. The *Herschel* spacecraft was designed, built, tested, and launched under a contract to ESA managed by the *Herschel*/Planck Project team by an industrial consortium under the overall responsibility of the prime contractor Thales Alenia Space (Cannes), and including Astrium (Friedrichshafen) responsible for the payload module and for system testing at spacecraft level, Thales Alenia Space (Turin) responsible for the service module, and Astrium (Toulouse) responsible for the telescope, with in excess of a hundred sub-contractors.

REFERENCES

Alves J., Lombardi M., Lada C. J., 2017, A&A, 606, L2
Anderson L. D., Bania T. M., Balser D. S., Cunningham V., Wenger T. V., Johnstone B. M., Armentrout W. P., 2014, ApJS, 212, 1
Battersby C. et al., 2011, A&A, 535, A128
Battersby C., Ginsburg A., Bally J., Longmore S., Dunham M., Darling J., 2014, ApJ, 787, 113
Benjamin R. A. et al., 2003, PASP, 115, 953
Berry D. S., 2015, Astron. Comput., 10, 22
Beuther H., Steinacker J., 2007, ApJ, 656, L85
Bintley D., et al., 2014, Millimeter, Submillimeter, and Far-Infrared Detectors and Instrumentation for Astronomy VII. SPIE, Bellingham, p. 915303
Burkhart B., Ossenkopf V., Lazarian A., Stutzki J., 2013, ApJ, 771, 122
Butler M. J., Tan J. C., 2012, ApJ, 754, 5
Carey S. J., Clark F. O., Egan M. P., Price S. D., Shipman R. F., Kuchar T. A., 1998, ApJ, 508, 721
Carey S. J. et al., 2009, PASP, 121, 76
Chandrasekhar S., Fermi E., 1953, ApJ, 118, 113
Churchwell E. et al., 2006, ApJ, 649, 759
Churchwell E. et al., 2009, PASP, 121, 213
Clarke S. D., Whitworth A. P., Hubber D. A., 2016, MNRAS, 458, 319
Clemens D. P., 1985, ApJ, 295, 422
Dempsey J. T., Thomas H. S., Currie M. J., 2013, ApJS, 209, 8
Donkov S., Veltchev T. V., Klessen R. S., 2012, MNRAS, 423, 889
Eden D. J., Moore T. J. T., Plume R., Morgan L. K., 2012, MNRAS, 422, 3178
Eden D. J., Moore T. J. T., Morgan L. K., Thompson M. A., Urquhart J. S., 2013, MNRAS, 431, 1587
Eden D. J. et al., 2017, MNRAS, 469, 2163
Egan M. P., Shipman R. F., Price S. D., Carey S. J., Clark F. O., Cohen M., 1998, ApJ, 494, L199
Elia D. et al., 2010, A&A, 518, L97
Elmegreen B. G., 2011, ApJ, 731, 61
Federrath C., Klessen R. S., 2012, ApJ, 761, 156
Federrath C., Klessen R. S., 2013, ApJ, 763, 51
Federrath C., Klessen R. S., Schmidt W., 2008, ApJ, 688, L79
Federrath C., Roman-Duval J., Klessen R. S., Schmidt W., Mac Low M.-M., 2010, A&A, 512, A81
Fiege J. D., Pudritz R. E., 2000, MNRAS, 311, 85
Fuller G. A., Myers P. C., 1992, ApJ, 384, 523
Gutermuth R. A., Heyer M., 2015, AJ, 149, 64
Gutermuth R. A., Megeath S. T., Myers P. C., Allen L. E., Pipher J. L., Fazio G. G., 2009, ApJS, 184, 18
Guzmán A. E., Sanhueza P., Contreras Y., Smith H. A., Jackson J. M., Hoq S., Rathborne J. M., 2015, ApJ, 815, 130
Heiderman A., Evans N. J., II, Allen L. E., Huard T., Heyer M., 2010, ApJ, 723, 1019
Hennebelle P., Pérault M., Teyssier D., Ganesh S., 2001, A&A, 365, 598
Hennemann M. et al., 2010, A&A, 518, L84
Henning T., Linz H., Krause O., Ragan S., Beuther H., Launhardt R., Nielbock M., Vasyunina T., 2010, A&A, 518, L95
Henshaw J. D. et al., 2016, MNRAS, 463, 146
Holland W. S. et al., 2013, MNRAS, 430, 2513
Inutsuka S.-I., Miyama S. M., 1992, ApJ, 388, 392
Jackson J. M. et al., 2006, ApJS, 163, 145
Jackson J. M., Finn S. C., Chambers E. T., Rathborne J. M., Simon R., 2010, ApJ, 719, L185
Kainulainen J., Ragan S. E., Henning T., Stutz A., 2013, A&A, 557, A120
Kauffmann J., Pillai T., 2010, ApJ, 723, L7
Kauffmann J., Bertoldi F., Bourke T. L., Evans N. J., II, Lee C. W., 2008, A&A, 487, 993
Kauffmann J., Pillai T., Shetty R., Myers P. C., Goodman A. A., 2010, ApJ, 712, 1137
Kauffmann J., Pillai T., Goldsmith P. F., 2013, ApJ, 779, 185
Klessen R. S., Heitsch F., Mac Low M.-M., 2000, ApJ, 535, 887
Kritsuk A. G., Norman M. L., Padoan P., Wagner R., 2007, ApJ, 665, 416
Kritsuk A. G., Norman M. L., Wagner R., 2011, ApJ, 727, L20
Krumholz M. R., McKee C. F., 2005, ApJ, 630, 250
Krumholz M. R., McKee C. F., 2008, Nature, 451, 1082
Lada C. J., Lombardi M., Alves J. F., 2010, ApJ, 724, 687
Lombardi M., Alves J., Lada C. J., 2015, A&A, 576, L1
Mardones D., Myers P. C., Tafalla M., Wilner D. J., Bachiller R., Garay G., 1997, ApJ, 489, 719
McKee C. F., Holliman J. H., II, 1999, ApJ, 522, 313
McKee C. F., Tan J. C., 2003, ApJ, 585, 850
Molinari S., Pezzuto S., Cesaroni R., Brand J., Faustini F., Testi L., 2008, A&A, 481, 345
Molinari S. et al., 2010, PASP, 122, 314
Molinari S. et al., 2016a, A&A, 591, A149
Molinari S., Merello M., Elia D., Cesaroni R., Testi L., Robitaille T., 2016b, ApJ, 826, L8
Moore T. J. T. et al., 2015, MNRAS, 453, 4264
Myers P. C., Mardones D., Tafalla M., Williams J. P., Wilner D. J., 1996, ApJ, 465, L133
Nagasawa M., 1987, Prog. Theor. Phys., 77, 635
Ossenkopf V., Henning T., 1994, A&A, 291, 943
Ossenkopf-Okada V., Csengeri T., Schneider N., Federrath C., Klessen R. S., 2016, A&A, 590, A104
Padoan P., Nordlund Å., 2002, ApJ, 576, 870
Padoan P., Nordlund Å., 2011, ApJ, 730, 40
Padoan P., Nordlund A., Jones B. J. T., 1997a, MNRAS, 288, 145
Padoan P., Jones B. J. T., Nordlund Å. P., 1997b, ApJ, 474, 730

Passot T., Vázquez-Semadeni E., 1998, Phys. Rev. E, 58, 4501
Pomarès M. et al., 2009, A&A, 494, 987
Rathborne J. M., Jackson J. M., Simon R., 2006, ApJ, 641, 389
Rathborne J. M., Simon R., Jackson J. M., 2007, ApJ, 662, 1082
Rathborne J. M., Johnson A. M., Jackson J. M., Shah R. Y., Simon R., 2009, ApJS, 182, 131
Rathborne J. M., Garay G., Jackson J. M., Longmore S., Zhang Q., Simon R., 2011, ApJ, 741, 120
Rigby A. J. et al., 2016, MNRAS, 456, 2885
Roman-Duval J., Jackson J. M., Heyer M., Johnson A., Rathborne J., Shah R., Simon R., 2009, ApJ, 699, 1153
Saraceno P., Andre P., Ceccarelli C., Griffin M., Molinari S., 1996, A&A, 309, 827
Schneider N. et al., 2015, A&A, 578, A29
Simon R., Jackson J. M., Rathborne J. M., Chambers E. T., 2006, ApJ, 639, 227
Spitzer Science C., 2009, VizieR Online Data Catalog, 2293
Tan J. C., Kong S., Butler M. J., Caselli P., Fontani F., 2013, ApJ, 779, 96
Tomisaka K., 1995, ApJ, 438, 226
Traficante A., Fuller G. A., Peretto N., Pineda J. E., Molinari S., 2015, MNRAS, 451, 3089
Tremblin P., Audit E., Minier V., Schmidt W., Schneider N., 2012, A&A, 546, A33
Tremblin P. et al., 2014, A&A, 564, A106
Urquhart J. S. et al., 2007, A&A, 474, 891
Urquhart J. S. et al., 2009, A&A, 501, 539
Vazquez-Semadeni E., 1994, ApJ, 423, 681
Vázquez-Semadeni E., González R. F., Ballesteros-Paredes J., Gazol A., Kim J., 2008, MNRAS, 390, 769
Veltchev T. V., Klessen R. S., Clark P. C., 2011, MNRAS, 411, 301
Wang Y., Zhang Q., Rathborne J. M., Jackson J., Wu Y., 2006, ApJ, 651, L125
Wang Y., Zhang Q., Pillai T., Wyrowski F., Wu Y., 2008, ApJ, 672, L33
Wang K. et al., 2014, MNRAS, 439, 3275
Williams G. M., Peretto N., Avison A., Duarte-Cabral A., Fuller G. A., 2018, A&A, 613, A11
Yuan J. et al., 2017, ApJS, 231, 11
Yuan J. et al., 2018, ApJ, 852, 12
Zhang C.-P., Yuan J.-H., Li G.-X., Zhou J.-J., Wang J.-J., 2017, A&A, 598, A76

APPENDIX: CO SPECTRA OF ALL CLUMPS

Fig. A1 shows the spectra of ^{12}CO, ^{13}CO, and C^{18}O (3–2) of all 27 clumps. For clumps with ^{13}CO/C^{18}O (3–2) intensity higher than 2.4 K (3σ of the main-beam efficiency corrected CHIMPS data, shown by grey dashed lines), we fit the line profile with a Gaussian function and derive the centre velocity and line width. Blue dashed lines show the fitted centre velocities of ^{13}CO, and green dashed lines show the fitted centre velocities of C^{18}O for each clump. Only for Clumps 20 and 22, centre velocities of ^{13}CO deviate from centre velocities of C^{18}O, which indicates that ^{13}CO might be self-absorbed. The evolutionary classes are labelled at the top right.

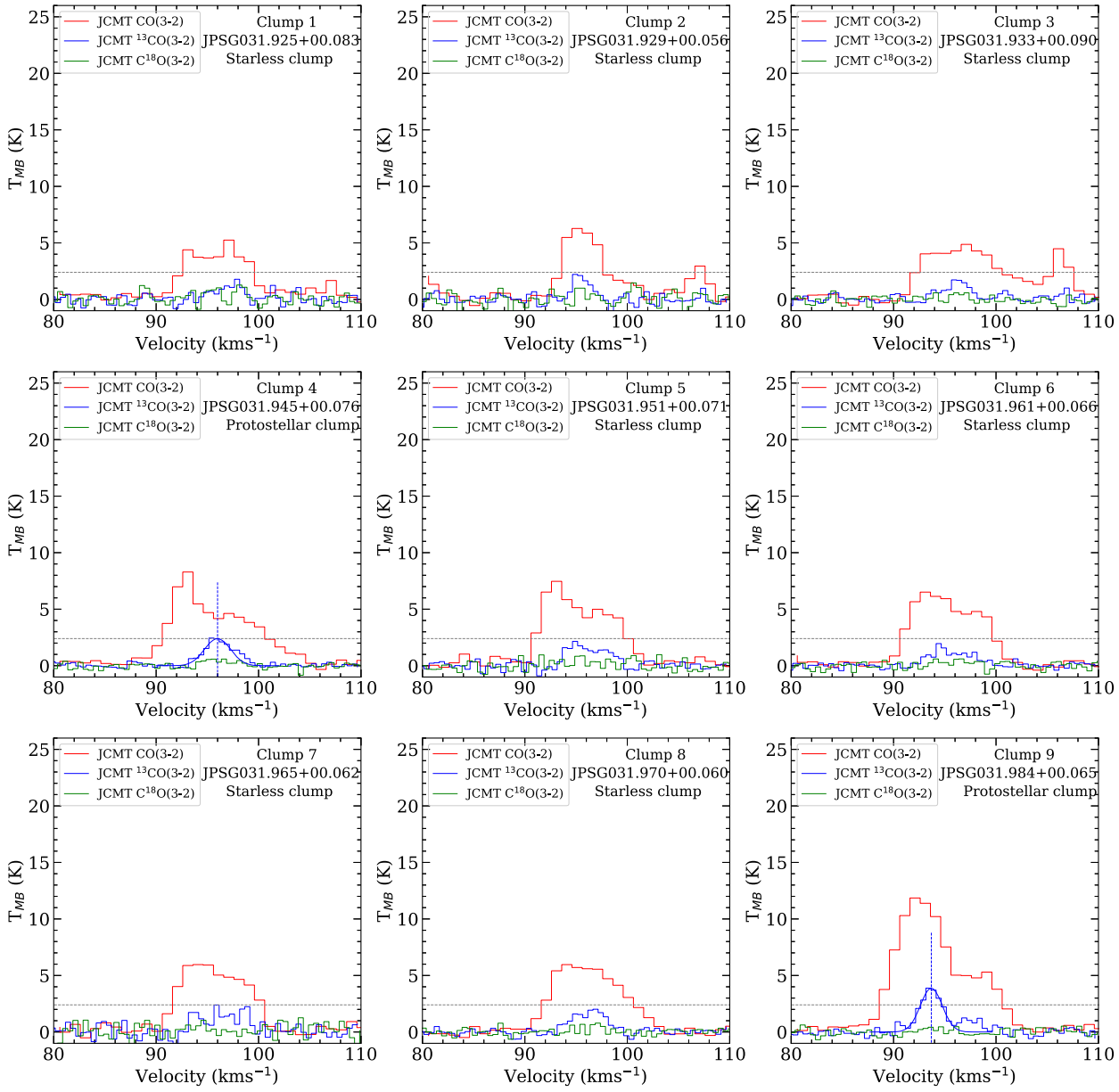

Figure A1. ^{12}CO, ^{13}CO, and C^{18}O (3–2) spectra of each clump. For each plot, the lines of ^{12}CO, ^{13}CO, and C^{18}O (3–2) are coloured red, blue, and green, respectively. Grey dashed lines show the 3σ threshold of main-beam efficiency corrected CHIMPS data (∼2.4 K). Blue dashed lines show the fitted centre velocities of ^{13}CO, and green dashed lines show the fitted centre velocities of C^{18}O for each clump. The evolutionary classes are labelled at the top right.

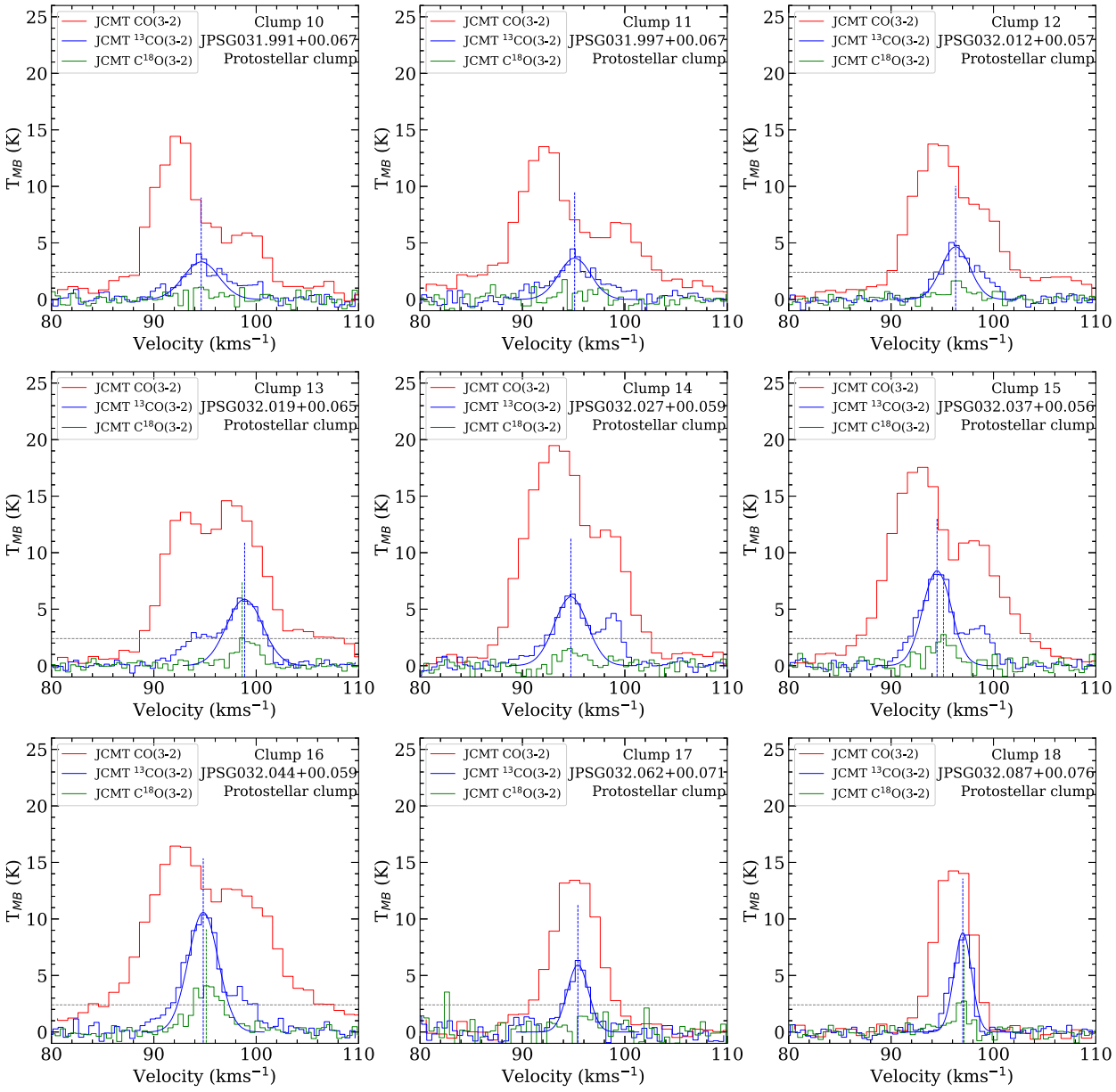

Figure A1 – *continued*

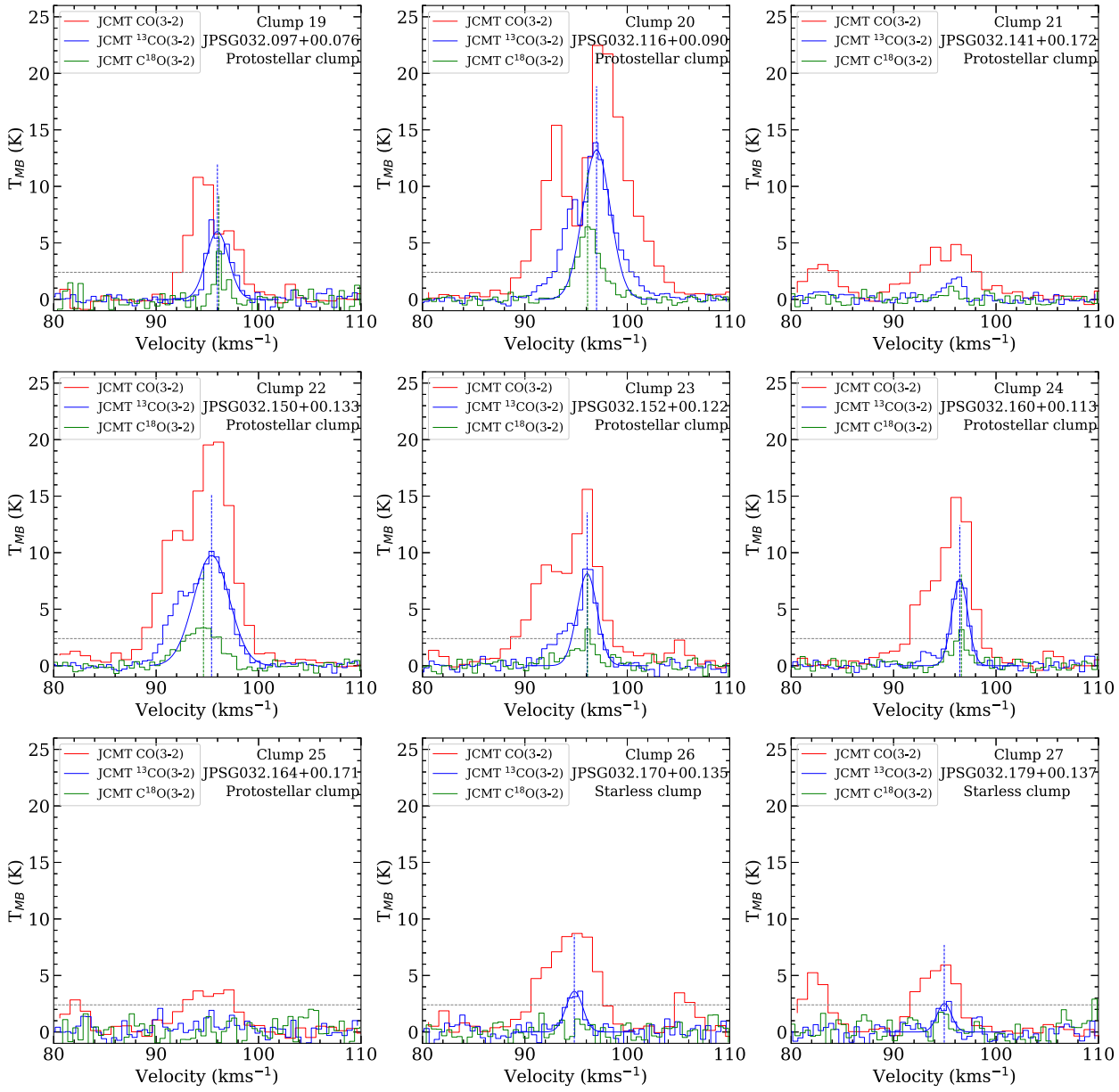

Figure A1 – *continued*

This paper has been typeset from a TEX/LATEX file prepared by the author.